

---

Doctoral Dissertations

Student Theses and Dissertations

---

Spring 2009

## Modeling and simulation of high pressure composite cylinders for hydrogen storage

Jianbing Hu

Follow this and additional works at: [https://scholarsmine.mst.edu/doctoral\\_dissertations](https://scholarsmine.mst.edu/doctoral_dissertations)



Part of the [Mechanical Engineering Commons](#)

Department: Mechanical and Aerospace Engineering

---

### Recommended Citation

Hu, Jianbing, "Modeling and simulation of high pressure composite cylinders for hydrogen storage" (2009). *Doctoral Dissertations*. 1941.

[https://scholarsmine.mst.edu/doctoral\\_dissertations/1941](https://scholarsmine.mst.edu/doctoral_dissertations/1941)

This thesis is brought to you by Scholars' Mine, a service of the Missouri S&T Library and Learning Resources. This work is protected by U. S. Copyright Law. Unauthorized use including reproduction for redistribution requires the permission of the copyright holder. For more information, please contact [scholarsmine@mst.edu](mailto:scholarsmine@mst.edu).



**MODELING AND SIMULATION OF HIGH PRESSURE COMPOSITE  
CYLINDERS FOR HYDROGEN STORAGE**

by

**JIANBING HU**

**A DISSERTATION**

**Presented to the Faculty of the Graduate School of the  
MISSOURI UNIVERSITY OF SCIENCE AND TECHNOLOGY**

**In Partial Fulfillment of the Requirements for the Degree**

**DOCTOR OF PHILOSOPHY  
IN MECHANICAL ENGINEERING**

**2009**

**Approved by**

**K. Chandrashekhara, Advisor  
Lokeswarappa R. Dharani  
Hai-Lung Tsai  
Gregory E. Hilmas  
William E. Showalter**

© 2009

Jianbing Hu

All Rights Reserved

## **PUBLICATION DISSERTATION OPTION**

This dissertation has been prepared in the form of three papers for publication as follows:

Pages 7-47 have been published in *ADVANCED COMPOSITE MATERIALS*.

Pages 48-87 have been published in *INTERNATIONAL JOURNAL OF HYDROGEN ENERGY*.

Pages 88-128 intended to submit to *INTERNATIONAL JOURNAL OF HYDROGEN ENERGY*.

## ABSTRACT

Composite hydrogen cylinders provide an efficient means of storage of hydrogen gas for modern hydrogen vehicles. Safety issues arising from the high gas pressure, temperature variation, fire attack, and fracture failures are the main concerns. The focus of this study is to develop a Finite Element (FE) model to predict the performance of composite cylinders subjected to extreme mechanical/thermal loadings and provide guidance for design optimization. In the first part of this work, a predictive FE model of composite cylinders has been developed considering various mechanical and thermal loadings. Doubly-curved laminated shell theory, accounting for transverse shear deformation and geometric nonlinearity, is used to model the composite cylinder wall. A back-propagation Neural Network (NNk) model, which is capable of predicting the failure pressure for arbitrarily specified loading conditions, has been developed. Also, the failure types and effects of thermal loading are investigated. In the second part, a comprehensive FE model has been developed to predict the behavior of the cylinder subjected to flame impingements. A failure model based on Hashin's theory has been implemented to detect various failure modes of the composite. Damage due to resin burn-out and mechanical degradation are also considered in the model. Numerical results are presented for thermal damage, residual properties and resin content profile of the cylinder. In the third part, fracture behavior of the cylinder with an axial surface crack in the liner has been studied using fracture mechanics and a global-local FE technique with consideration of autofrettage effect. Results on the fracture parameters (K and J-integral) with various autofrettage levels, crack sizes and crack shapes are presented.

## ACKNOWLEDGMENTS

The author wishes to extend his deepest gratitude to his academic advisor, Dr. K. Chandrashekhara, for his continued guidance, advice, encouragement and financial support throughout the course of the investigation and successful completion of this dissertation research.

The author also wishes to extend his greatest appreciation to the members of the advisory committee, Dr. Lokeswarappa. R. Dharani, Dr. Hai-Lung Tsai, Dr. Gregory E. Hilmas, and Dr. William E. Showalter for their advice and encouragement, and their time and effort for review of this dissertation.

Many thanks go to Dr. S. Sundararaman for his prior input in this research. The author also appreciates the assistance from his fellow colleagues and friends, Mr. Jian Chen, Mr. V.G.K. Menta and Mr. R. Vuppalapati.

The author would like to take this opportunity to thank Mr. William Chernicoff of the US Department of Transportation for his assistance with information and ideas. The funding of this research by the US Department of Transportation is gratefully acknowledged.

The author would also like to acknowledge the financial support received from the Department of Mechanical and Aerospace Engineering at Missouri S&T for Graduate Research Assistantship and Graduate Teaching Assistantship.

Finally, the author wishes to express his deepest gratitude to his parents, his sisters and brothers-in-law for their understanding, patience, encouragement, support, and for helping realize and accomplish his dreams.

## TABLE OF CONTENTS

	Page
PUBLICATION DISSERTATION OPTION .....	iii
ABSTRACT .....	iv
ACKNOWLEDGMENTS .....	v
LIST OF ILLUSTRATIONS .....	ix
LIST OF TABLES .....	xi
SECTION	
1. INTRODUCTION .....	1
1.1. BACKGROUND .....	1
1.2. SCOPE AND OBJECTIVES .....	3
1.3. CONCLUDING REMARKS .....	5
PAPER	
I. FAILURE PRESSURE PREDICTION OF COMPOSITE CYLINDERS FOR HYDROGEN STORAGE USING THERMO-MECHANICAL ANALYSIS AND NEURAL NETWORK .....	7
ABSTRACT .....	7
1. INTRODUCTION .....	8
2. SHEAR DEFORMABLE SHELL THEORY .....	10
3. COMPOSITE FAILURE MODEL .....	13
4. MATERIAL PROPERTIES .....	14
5. FINITE ELEMENT SIMULATION .....	15
6. NEURAL NETWORK MODEL .....	17
7. RESULTS AND DISCUSSION .....	19
8. CONCLUSIONS .....	22
REFERENCES .....	23
II. ANALYSIS OF COMPOSITE HYDROGEN STORAGE CYLINDERS SUBJECTED TO LOCALIZED FLAME IMPINGEMENTS .....	48
ABSTRACT .....	48
1. INTRODUCTION .....	49
2. MODELING OF HIGH PRESSURE COMPOSITE HYDROGEN STORAGE CYLINDERS .....	51



2.1. Thermal Model .....	51
2.2. Sub-laminate Model .....	53
2.3. Formulation of Finite Element Model .....	55
3. MATERIAL MODELS .....	56
3.1. Temperature Dependent Material Properties .....	56
3.2. Composite Failure Criteria .....	57
3.3. Model for Hydrogen Gas .....	58
4. FINITE ELEMENT SIMULATION PROCEDURE .....	59
5. RESULTS AND DISCUSSION .....	60
6. CONCLUSIONS .....	62
REFERENCES .....	63
<b>III. FRACTURE ANALYSIS OF HYDROGEN STORAGE COMPOSITE CYLINDERS WITH LINER CRACK ACCOUNTING FOR AUTOFRETTAGE EFFECT .....</b>	<b>88</b>
ABSTRACT .....	88
1. INTRODUCTION .....	89
2. METHODOLOGY .....	91
2.1. Autofrettage Effect on High Pressure Composite Cylinder for Hydrogen Storage .....	91
2.2. Stress Intensity Factor (K) Evaluation .....	93
2.3. J-Integral Evaluation .....	94
2.4. Material Models .....	95
3. FINITE ELEMENT SIMULATION .....	97
3.1. Global Model .....	98
3.2. Local Model .....	99
3.3. Simulation Procedure .....	100
4. RESULTS AND DISCUSSION .....	101
4.1. Autofrettage Process Simulation .....	101
4.2. Stress Intensity Factor (K) and J-integral .....	102
4.3. Stress Field Characterization on the Crack Tip Vicinity .....	103
5. CONCLUSIONS .....	104
REFERENCES .....	105

SECTION	
BIBLIOGRAPHY .....	129
VITA .....	132

## LIST OF ILLUSTRATIONS

Figure	Page
<b>PAPER I</b>	
1. Structure scheme of hydrogen storage cylinder .....	34
2. Doubly curved shell and coordinate system .....	35
3. Finite element model of hydrogen cylinder .....	36
4. Feedforward back-propagation Neural Network architecture .....	37
5(a). Uniform thermal loading with $T_{in}=T_{out}$ (in Case 1) .....	38
5(b). Uniform thermal loading $T_{in}=T_{out}$ (in Case 2) .....	39
5(c). Uniform thermal loading $T_{in}=T_{out}$ (in Case 3) .....	40
6(a). Gradient thermal loading with $T_{out}=50^{\circ}\text{C}$ (in Case 1) .....	41
6(b). Gradient thermal loading with $T_{out}=50^{\circ}\text{C}$ (in Case 2) .....	42
6(c). Gradient thermal loading with $T_{out}=50^{\circ}\text{C}$ (in Case 3) .....	43
7. Failure pressure with inside temperature variation ( $T_{out}=25^{\circ}\text{C}$ ) .....	44
8. Ply-by-ply failure predictions under various thermal loadings .....	45
9(a). Comparison of failure pressures from NNk and ABAQUS at $\theta = 15^{\circ}$ .....	46
9(b). Comparison of failure pressures from NNk and ABAQUS at $\theta = 25^{\circ}$ .....	47
<b>PAPER II</b>	
1. Schematic of hydrogen cylinder .....	73
2. Curve fitting for hydrogen gas state equation at constant density .....	74
3. Finite element model of the cylinder .....	75
4. Stacking sequence of the cylinder wall .....	76
5. Finite element implementation schemes .....	77
6. Variation of sink temperature with film coefficient .....	78
7. Internal pressure variation with time for various flame area sizes .....	79
8. Temperature distributions along the length at inner surface of the aluminum liner .....	80
9. Temperature distributions through composite thickness .....	81
10. Residual resin content through the thickness .....	82
11. Stress ( $S_{11}$ ) distribution through the thickness .....	83
12. Stress ( $S_{22}, S_{33}$ ) distribution through the thickness .....	84
13(a). Fiber fracture index ( $I_{mt}$ ) contour around heat source .....	85

13(b). Matrix cracking index ( $I_{ft}$ ) contour around heat source .....	86
13(c). Density index ( $\rho/\rho_0$ ) contour around heat source .....	87
<b>PAPER III</b>	
1. Schematic of hydrogen composite cylinder .....	112
2. Diagram of autofrettage process .....	113
3. Schematic of domain integral evaluation .....	114
4. Global finite element model .....	115
5. Local finite element model .....	116
6. Implementation scheme .....	117
7. von-Mises stress distribution in liner .....	118
8. Cyclic stress-strain curves for various autofrettage levels .....	119
9. Stress intensity factor (K) along crack front for various autofrettage levels .....	120
10. J-integral along crack front for various autofrettage levels .....	121
11. Stress intensity factor (K) against pressure loading for various autofrettage levels .....	122
12. J-integral against pressure loading for various autofrettage levels .....	123
13. Stress intensity factor (K) along crack front with various geometric ratios .....	124
14. J-integral along crack front with various geometric ratios .....	125
15. Stress distribution of the crack front vicinity .....	126
16. Transition of plastic zone shapes along crack front .....	127
17. Plastic zone shapes for various autofrettage levels .....	128

## LIST OF TABLES

Table	Page
<b>PAPER I</b>	
1. Ultimate strength of carbon/epoxy composite .....	27
2. Mechanical and thermal properties of S-glass/epoxy .....	28
3. Mechanical and thermal properties of Aluminum Alloy 6061-T6 .....	29
4. Lay-up configurations for various winding patterns .....	30
5. Weights and biases for trained neural network .....	31
6. Scale constants for trained neural network .....	32
7. Testing cases and maximum error of prediction .....	33
<b>PAPER II</b>	
1. Curve fitting parameters for transverse and shear modulus .....	67
2. Thermal expansion coefficients of carbon/epoxy .....	68
3. Specific heat and thermal conductivity of carbon/epoxy .....	69
4. Parameters for resin reaction model .....	70
5. Strength of carbon/epoxy .....	71
6. Design parameters for the cylinder .....	72
<b>PAPER III</b>	
1. Mechanical properties of carbon/epoxy composite .....	110
2. Mechanical properties of Aluminum Alloy 7075-T651 .....	111

# 1. INTRODUCTION

## 1.1. BACKGROUND

Currently, the energy crisis and environmental pollution arising from burning fossil fuel in vehicles are identified as some of the major concerns in the global world. Hydrogen, a renewable and clean energy resource, is a promising substitute for fossil fuels. One of the key challenges for the usage of hydrogen gas in automobiles is to develop a compact and efficient way of hydrogen storage. The solutions for this challenge can be categorized into three main groups [1-2]: (a) Cryogenic hydrogen storage: It provides high volumetric density (0.07 kg/L) and good weight density (2.8 %), but liquefaction (-423.2 °F) is an intensive energy consuming process and evaporation reduces the gas usage efficiency. (b) Hydrogen storage materials: Traditional metallic hydrogen storage materials provide a safe way to store hydrogen gas, but a low weight density (1.4 %) and operation complexity prohibit it from practical applications. Recently, carbon nano-tubes have attracted much research interest as a future hydrogen storage material, but it still remains in the early investigation phase [3]. (c) Compressed hydrogen gas: It is expected to be the main stream for hydrogen storage in the near future as it provides good volumetric and weight density (0.03 kg/L and 6%) and simplicity of transportation and storage.

Traditionally, compressed hydrogen gas is stored in metallic cylinders (Type I cylinder). The storage pressure for this type of cylinder is low (usually less than 25 MPa) and the capacity of hydrogen gas storage is limited. Also, hydrogen embrittlement can result in micro-cracks and reduce the strength of the cylinder. The Type II cylinder is developed by wrapping fiber-reinforced composite materials in the hoop direction on the metallic cylinder [4]. It reduces the weight of the cylinder significantly. However, this still does not meet the requirement of hydrogen storage capacity for automobiles. To further reduce the weight and increase the storage capacity, fully wrapped composite cylinders (Type III and Type IV) have been introduced. The cylinders are manufactured by the filament winding technique. In this process, a liner is used as a mandrel and the high strength, low density composite (fiber strength 5-6 GPa, composite density 1.6 g/cm<sup>3</sup>) is fully wrapped in both the helical and the hoop directions. The helical winding

produces helical layers to bear the axial loading, while the hoop winding generates hoop layers to carry circumferential loading. The liner serves as a gas barrier after the cylinder is manufactured. The Type III differentiates the Type IV by the material used for the liner (aluminum for Type III and polymer for Type IV). To obtain efficient storage capacity, the cylinders are designed for pressures as high as 5,000 to 10,000 psi and, hence, the failure of the cylinder would lead to a catastrophic accident. In this context, safe installation and operation of high-pressure composite cylinders for hydrogen storage are of primary concern. To design the cylinder with the highest possible safety, reliability and minimum weight considerations, mechanics relevant to the behavior of the cylinder must be well understood.

The early technique used for analyzing filament-wound composite cylinders is netting analysis [5-7]. This procedure has been widely used in the industry for its simplicity. A static equilibrium principle is applied to obtain the stress on the fiber by neglecting the contribution of the resin matrix. Although this technique provides a concise way to predetermine some design parameters for cylinder prototypes, more detailed analysis is necessary for examining and optimizing the high pressure composite cylinder for hydrogen storage under various operating conditions.

Considering the effect of resin matrix, many studies have been focused on developing an analytical solution for composite cylinders under various loadings. Lekhnitskii [8] laid the foundation for analyzing the anisotropic elasticity. Numerous authors [9-13] advanced the model for the stress analysis of cylinders under uniaxial, biaxial and combined centrifugal pressure loadings in terms of stress functions. Later on, based on a plain-strain assumption, Akcay and Kaynak [14] analyzed closed-end cylinders under uniform thermal loading. Sayman [15] incorporated a general hydrothermal effect in the model that is suitable for multi-layered thin/thick composite cylinders for the axially symmetric case under uniform or parabolic temperature distributions. Tabakov [16] developed a model to obtain exact solutions for the thick laminated anisotropic cylinder with closed ends, but this model was limited to five layers and was not universal. In his later work [17], a general model was developed by deriving the governing differential equations instead of stress functions without considering the end effects and closing

plates. More recently, Chapelle and Perreux [18] extended the analytical method to analyzing a Type III hydrogen cylinder by including plastic flow of the liner.

The Finite Element Method (FEM) provides a convenient tool to analyze composite cylinders with consideration of nonlinearities, failure modes and various loading conditions. A three dimensional finite element was developed by Hoa et al. [19] for the strain analysis of fiber reinforced plastic vessels containing discontinuities such as manhole connections or nozzles. Considering the change of winding angles through the thickness of helical laminates, finite element analyses were performed by Park et al. [20] through coding the winding angle to each solid element. Kabir [21] modeled the structure of the cylinder wall as an elastic, ideally plastic liner, reinforced with quasi-isotropic elastic composite. Tam et al. [22] analyzed the composite tank considering both material and geometric nonlinearities. Gray and Moser [23] described a method which has been developed to analyze filament-wound composite pressure vessels accounting for the highly orthotropic nature of vessel structures. Kim et al. [24] employed a 3-D element to compute stresses for optimizing the composite pressure vessel design. In addition, significant studies were conducted by several researchers [25-28] on the analysis of composite pressure vessels with incorporating failure and progressive damage models in FE programs. The fracture and fatigue behavior of composite pipes and cylinders have also been investigated by many authors [29-34] using both stress/strain criteria and direct crack-modeling techniques in finite element models.

## **1.2. SCOPE AND OBJECTIVES**

Based on the literature survey, many researchers have used finite element method on the study of composite vessels or pipes, but there is no significant research on the analysis of Type III cylinders subjected to thermo-mechanical loading. In the case of fire impingements, the previous studies have been carried out on flat composite panels and lack the capability of analyzing composite cylinders considering both mechanical and thermal damage. Furthermore, fracture failure is another essential factor for the safety and design life-expectancy of the cylinder. Most of the previous studies have performed fracture analysis either on compressed natural gas cylinders or on pressure vessels used for aerospace. Intensive analysis has been conducted on metallic cylinders and a few are



related to cylinders with a metallic liner wrapped by composites. However, not much research has been performed on composite hydrogen cylinders with consideration of the autofrettage effect.

As an effort to develop the finite element model to predict the behavior of Type III hydrogen cylinders for the safety concern and design guidance, this study focuses on three aspects. The first one is to develop a finite element model that can predict the failure pressure of the cylinder subjected to combined thermal and mechanical loadings. The second one is to develop a comprehensive finite element model that can identify failure modes of the cylinder when it is attacked by fire impingement. The third one is to evaluate the performance of the cylinder containing liner cracks from the perspective view of fracture mechanics using finite element simulation technique.

This dissertation has been prepared in the form of three parts corresponding to the addressed problems.

The first part is titled “**Failure Pressure Prediction of Composite Cylinders for Hydrogen Storage using Thermo-mechanical Analysis and Neural Network.**” In this part, a finite element simulation tool for the design of hydrogen storage cylinders has been developed. The structural response of the cylinder is analyzed using laminated shell theory accounting for transverse shear deformation and geometric nonlinearity. A composite failure model is used to evaluate the failure pressure. A back-propagation Neural Network model is developed based on the results of finite element analysis to predict the maximum failure pressure for arbitrary thermo-mechanical loading conditions.

The second part is titled “**Analysis of Composite Hydrogen Storage Cylinders Subjected to Localized Flame Impingements.**” In this part, a comprehensive non-linear finite element model has been developed for predicting the behavior of composite hydrogen storage cylinders subjected to high pressure and localized flame impingements. The model is formulated in an axi-symmetric coordinate system and incorporates various sub-models to capture the behavior of the composite cylinder under extreme thermo-mechanical loadings. Sub-models are implemented in ABAQUS commercial finite element code using user subroutines. Numerical results are presented for thermal damage, residual properties and profile of resin content of the cylinder wall.

The third part is titled “**Fracture Analysis of Hydrogen Storage Composite Cylinders with Liner Crack accounting for Autofrettage Effect.**” In this part, a global-local finite element model is developed to investigate the axial surface flaws in the liner of high pressure composite cylinders for hydrogen storage using fracture mechanics. The effect of autofrettage process is studied due to its strong influence on the cylinder fracture behavior. The autofrettage process simulation is conducted in the global model. The local model, which is driven by the results of the global model, performs a detailed analysis of the crack to assure accurate computation of fracture parameters. Results of both stress intensity factor (K) and J-integral are reported along the crack front in four autofrettage levels and with different crack sizes. The plastic zone along the crack front is also studied.

### **1.3. CONCLUDING REMARKS**

In the first part, a doubly curved shell model accounting for transverse shear deformation is used for the thermo-mechanical analysis of hydrogen composite storage cylinders. Temperature dependent material properties of the load carrying carbon/epoxy layer and geometry nonlinearity are also considered in the numerical model. Under uniform thermal loading, a temperature increase significantly raises the maximum failure pressure based on the Tsai-Wu failure criterion. Contrastively, the non-uniform thermal loading can cause an uneven load distribution and hence decrease the maximum failure pressure. The thickness ratio also plays an important role in determining the maximum failure pressure and should be selected appropriately based on the thermal and mechanical loading conditions. A neural network model is developed and used to predict the failure pressure. The performance of the trained neural network is then evaluated by comparing the predicted values with those of testing cases. The results are in good agreement.

In the second part, a comprehensive finite element model has been developed to analyze composite hydrogen storage cylinders subjected to high pressure and flame impingements. The model considers the resin reaction, heat exchange between the hydrogen gas and liner, and the progressive failure process. A sub-laminate model has been developed to reduce computational time. A temperature dependent material model

along with a failure model has been developed and implemented to accurately predict various failure modes for the hydrogen storage cylinder. Analysis of a typical high pressure composite hydrogen cylinder under fire exposure is conducted by using the developed models. Parametric studies are done on heat exchange rate (between hydrogen gas and the liner) and the size of the flame source. Stresses, temperature profile and failure types are reported. The developed model can be used to accommodate various types of thermal and mechanical loadings, lamina stacking sequence, and lamina thickness to establish safe working conditions and design limits for hydrogen storage cylinders.

In the third part, a global-local finite element model has been developed to predict the fracture behavior of high pressure composite cylinders for hydrogen storage. Simulation of the autofrettage process is carried out in the global model. Plastic hardening and the Bauschinger effect are observed in the results. Both stress intensity factor (K) and J-integral are computed along the crack front in the local model with consideration of autofrettage influence and crack size effect. It is found that the autofrettage process significantly improves the cylinder fracture performance and the smaller crack size reduces the value of fracture parameters dramatically. The plastic zone around the crack tip is studied in terms of shape and size. The fracture behavior is discussed through observation of the plastic zone and the corresponding selection of parametric characterization is suggested.

The current research can be extended in several ways for future work. The developed Neural Network model for failure pressure prediction can be applied to optimization of composite lay-ups under arbitrary environmental temperature conditions. The second part of the model can be extended to multi-physics analysis by simulating the fluid field of hydrogen gas in the cylinder. Pressure release device can be designed based on the prediction of simulation to minimize the hazard of cylinder failure when subjected to accidental fire. The fracture model can be used as a tool for cylinder autofrettage process to obtain an optimum stress state to restrict crack growth in the liner. Also, the currently developed fracture model can be extended to predict the fatigue life of the cylinder and provide guidance for material selection and lay-up optimization of the composite wall to achieve premium fracture performance.

**PAPER I:****FAILURE PRESSURE PREDICTION OF COMPOSITE CYLINDERS FOR  
HYDROGEN STORAGE USING THERMO-MECHANICAL ANALYSIS AND  
NEURAL NETWORK****ABSTRACT**

Safe installation and operation of high-pressure composite cylinders for hydrogen storage are of primary concern. It is unavoidable for the cylinders to experience temperature variation, and significant thermal input (or flux) during the service. The maximum failure pressure that the cylinder can sustain must be affected due to the nature of temperature dependent composites, integrity of the matrix and fibers and complexity of the cylinder design. Most of the analysis reported in high-pressure composite cylinders is based on simplified assumptions and does not account for complexities like thermo-mechanical behavior and temperature dependent material properties. In the present work, a comprehensive finite element simulation tool for the design of a hydrogen storage cylinder is developed. The structural response of the cylinder is analyzed using laminated shell theory accounting for transverse shear deformation and geometric nonlinearity. A composite failure model is used to evaluate the failure pressure under various thermo-mechanical loadings. A back-propagation Neural Network (NNk) model is developed to predict the maximum failure pressure using the analysis results. The failure pressures predicted from the NNk model are compared with those from testing cases. The developed NNk model is capable of predicting the failure pressure for any given loading condition.

## 1. INTRODUCTION

Composite high-pressure cylinders have potential application as hydrogen storage systems in automotive, transportation, portable, and stationary storage systems due to their light weight, simplicity of the storage and low cost for storage and transport of hydrogen gas [1]. Typically, a composite high-pressure cylinder is made of a high molecular weight polymer or aluminum liner that serves as a hydrogen gas permeation barrier. A filament-wound, carbon/epoxy composite laminate over-wrapped outside of the liner provides the desired pressure load bearing capacity [2]. A vehicle fuel system cylinder is capable of sustaining pressures of 5,000 psi or higher by taking advantage of the high strength and low specific weight of modern high performance composites. In addition, the maturation of the filament winding manufacturing process further reduces the price to being practical and common for use in mass transportation systems.

To design composite high-pressure cylinders with the highest possible safety, reliability and minimum weight considerations, the behavior of composite structures under various mechanical and thermal loadings, including localized and non-localized flames, needs to be well understood. Studies have been conducted by various researchers [3-5] on the structure of hydrogen composite cylinders under mechanical loadings. Using finite element method as a powerful numerical tool, numerous studies have been conducted on high-pressure cylinder analysis [6-8]. Compared to pure mechanical loading, fewer studies have been conducted on hydrogen composite cylinders subjected to thermal loads and combined thermo-mechanical loads [9, 10].

In the present study, a thermo-mechanical finite element model has been developed for the analysis of hydrogen storage cylinders. The composite laminate wall of hydrogen

composite cylinder typically consists of helical and hoop laminated layers. Both these layers, along with an aluminum liner, are considered for the analysis. During service, hydrogen composite cylinders unavoidably experience various thermal loadings combined with high inner pressure. To account for working temperature variation in the service, uniform temperature loadings ranging from 25°C to 140°C are considered for the analysis, above which the matrix begins to burn. During the gas filling process, the inner temperature can go up to around 100 °C [10]. Hence, non-uniform thermal loadings have also been included in the study. The variation of material properties with temperature is significant for most composites. A temperature dependent material model has been developed and implemented in commercial finite element code ABAQUS, using user subroutines. A laminated shell theory [11, 12] accounting for out-of-plane shear strains and geometric nonlinearity is used for the analysis.

When considering the combination of various thermal loadings, winding angles and lay up configurations in the analysis, it is a tremendous task to optimize the cylinder design and predict maximum failure pressure through case-by-case simulation. A back-propagation Neural Network (NNk) model is then developed to predict the failure pressure using the results from a few typical finite element simulation cases. The training process consists of training the network with three sets of simulation results with various winding angles and thermal loadings. Once trained, the developed NNk model can be used for guidance and optimization of hydrogen cylinder design. Some testing cases, which are not included in the training sets, are utilized to compare with the predicted failure pressure from the NNk model. A good agreement is found between failure pressures from testing cases and NNk model prediction.

## 2. SHEAR DEFORMABLE SHELL THEORY

A schematic of a hydrogen composite cylinder wall is shown in Figure 1. The inner liner is made of high molecular weight polymer or aluminum that serves as a hydrogen gas permeation barrier. A filament-wound, carbon/epoxy composite laminate over-wrapped on the outside of the liner provides the desired pressure load bearing capacity [13]. In many current designs, a glass/epoxy layer is placed over the carbon/epoxy laminate to provide impact and damage resistance. The doubly curved shell theory accounting for out of plane shear deformations and geometric nonlinearity is used for the analysis of composite hydrogen storage cylinders.

A multilayered doubly curved shell is shown in Figure 2. The curved coordinated system  $\{\xi_1, \xi_2, \zeta\}$  is used in space description. The coordinates  $\xi_1$  and  $\xi_2$  specify the position on the middle surface, while  $\zeta$  measures the distance, along the outward normal, from the mid-surface to an arbitrary point on the shell. The displacement field can be written as:

$$u(\xi_1, \xi_2, \zeta) = \left(1 + \frac{\zeta}{R_1}\right) u_o(\xi_1, \xi_2) + \zeta \phi_1(\xi_1, \xi_2) \quad (1.a)$$

$$v(\xi_1, \xi_2, \zeta) = \left(1 + \frac{\zeta}{R_2}\right) v_o(\xi_1, \xi_2) + \zeta \phi_2(\xi_1, \xi_2) \quad (1.b)$$

$$w(\xi_1, \xi_2, \zeta) = w_o(\xi_1, \xi_2) \quad (1.c)$$

The non-linear strain-displacement relations based on Sanders's shell theory can be given as:

$$\begin{aligned} \varepsilon_x &= \varepsilon_x^o + \zeta \kappa_x ; & \varepsilon_y &= \varepsilon_y^o + \zeta \kappa_y \\ \gamma_{xy} &= \gamma_{xy}^o + \zeta \kappa_{xy} ; & \gamma_{yz} &= \gamma_{yz}^o ; & \gamma_{xz} &= \gamma_{xz}^o \end{aligned} \quad (2)$$

where  $\varepsilon_j^0$  and  $\kappa_j$  are defined as:

$$\begin{aligned}
\varepsilon_x^0 &= \frac{1}{\alpha_1} \frac{\partial \mathbf{u}_o}{\partial \xi_1} + \frac{\mathbf{w}_o}{R_1} + \frac{1}{2\alpha_1^2} \left( \frac{\partial \mathbf{w}_o}{\partial \xi_1} \right)^2 ; \quad \kappa_x = \frac{1}{\alpha_1} \frac{\partial \phi_1}{\partial \xi_1} \\
\varepsilon_y^0 &= \frac{1}{\alpha_2} \frac{\partial \mathbf{v}_o}{\partial \xi_2} + \frac{\mathbf{w}_o}{R_2} + \frac{1}{2\alpha_2^2} \left( \frac{\partial \mathbf{w}_o}{\partial \xi_2} \right)^2 ; \quad \kappa_y = \frac{1}{\alpha_2} \frac{\partial \phi_2}{\partial \xi_2} \\
\gamma_{xy}^0 &= \frac{1}{\alpha_1} \frac{\partial \mathbf{v}_o}{\partial \xi_1} + \frac{1}{\alpha_2} \frac{\partial \mathbf{u}_o}{\partial \xi_2} + \frac{1}{2\alpha_1\alpha_2} \frac{\partial \mathbf{w}_o}{\partial \xi_1} \frac{\partial \mathbf{w}_o}{\partial \xi_2} ; \quad \gamma_{yz}^0 = \frac{1}{\alpha_2} \frac{\partial \mathbf{w}_o}{\partial \xi_2} + \phi_2 - \frac{\mathbf{v}_o}{R_2} \\
\gamma_{xz}^0 &= \frac{1}{\alpha_1} \frac{\partial \mathbf{w}_o}{\partial \xi_1} + \phi_1 - \frac{\mathbf{u}_o}{R_1} \\
\kappa_{xy} &= \frac{1}{\alpha_1} \frac{\partial \phi_2}{\partial \xi_1} + \frac{1}{\alpha_2} \frac{\partial \phi_1}{\partial \xi_2} - c_0 \left( \frac{1}{\alpha_1} \frac{\partial \mathbf{v}_o}{\partial \xi_1} - \frac{1}{\alpha_2} \frac{\partial \mathbf{u}_o}{\partial \xi_2} \right) \\
c_0 &= \frac{1}{2} \left( \frac{1}{R_1} - \frac{1}{R_2} \right); \quad dx = \alpha_1 d\xi_1; \quad dy = \alpha_2 d\xi_2
\end{aligned} \tag{3}$$

In Eq. (3),  $u$  and  $v$  are the displacements in the direction of the tangents to the coordinate lines  $\xi_1$  and  $\xi_2$ , respectively,  $w$  is the displacement in the direction of the outward normal and  $\phi_1$  and  $\phi_2$  are the rotations.

The stress-strain relation, accounting for thermal effects, in the shell coordinates for a  $k^{\text{th}}$  layer can be expressed as [12]:

$$\begin{Bmatrix} \sigma_x \\ \sigma_y \\ \tau_{xy} \\ \tau_{yz} \\ \tau_{xz} \end{Bmatrix}_k = \begin{bmatrix} Q_{11} & Q_{12} & Q_{16} & 0 & 0 \\ Q_{12} & Q_{22} & Q_{26} & 0 & 0 \\ Q_{16} & Q_{26} & Q_{66} & 0 & 0 \\ 0 & 0 & 0 & Q_{44} & Q_{45} \\ 0 & 0 & 0 & Q_{45} & Q_{55} \end{bmatrix}_k \begin{Bmatrix} \varepsilon_x - \alpha_x T \\ \varepsilon_y - \alpha_y T \\ \gamma_{xy} - \alpha_{xy} T \\ \gamma_{yz} \\ \gamma_{xz} \end{Bmatrix}_k \tag{4}$$

where  $Q_{ij}$  are the transformed elastic coefficients,  $T$  is the given temperature distribution,

and  $(\alpha_x, \alpha_y, \alpha_{xy})$  are the thermal expansion coefficients in the shell coordinates.



The laminate constitutive equations can be obtained by integrating Eq. (4) over the thickness, and is written as:

$$\begin{Bmatrix} N_x \\ N_y \\ N_{xy} \\ Q_{xz} \\ Q_{yz} \\ M_x \\ M_y \\ M_{xy} \end{Bmatrix} = \begin{bmatrix} A_{11} & A_{12} & A_{16} & 0 & 0 & B_{11} & B_{12} & B_{16} \\ A_{12} & A_{22} & A_{26} & 0 & 0 & B_{12} & B_{22} & B_{26} \\ A_{16} & A_{26} & A_{66} & 0 & 0 & B_{16} & B_{26} & B_{66} \\ 0 & 0 & 0 & A_{44} & A_{45} & 0 & 0 & 0 \\ 0 & 0 & 0 & A_{45} & A_{55} & 0 & 0 & 0 \\ B_{11} & B_{12} & B_{16} & 0 & 0 & D_{11} & D_{12} & D_{16} \\ B_{12} & B_{22} & B_{26} & 0 & 0 & D_{12} & D_{22} & D_{26} \\ B_{16} & B_{26} & B_{66} & 0 & 0 & D_{16} & D_{26} & D_{66} \end{bmatrix} \begin{Bmatrix} \varepsilon_x^0 \\ \varepsilon_y^0 \\ \gamma_{xy}^0 \\ \gamma_{xz}^0 \\ \gamma_{yz}^0 \\ \kappa_x \\ \kappa_y \\ \kappa_{xy} \end{Bmatrix} - \begin{Bmatrix} N_x^T \\ N_y^T \\ N_{xy}^T \\ 0 \\ 0 \\ M_x^T \\ M_y^T \\ M_{xy}^T \end{Bmatrix} \quad (5)$$

where  $N^T$  and  $M^T$  are thermal stress and moment resultants

$$(A_{ij} \quad B_{ij} \quad D_{ij}) = \int_{-h/2}^{h/2} Q_{ij} (1 \quad z \quad z^2) dz \quad (i, j = 1, 2, 6) \quad (6.a)$$

$$A_{ij} = \int_{-h/2}^{h/2} K_i K_j Q_{ij} dz \quad (i, j = 4, 5) \quad (6.b)$$

$$\begin{Bmatrix} N_x^T & M_x^T \\ N_y^T & M_y^T \\ N_{xy}^T & M_{xy}^T \end{Bmatrix} = \int_{-h/2}^{h/2} \begin{bmatrix} Q_{11} & Q_{12} & Q_{16} \\ Q_{12} & Q_{22} & Q_{26} \\ Q_{16} & Q_{26} & Q_{66} \end{bmatrix} \begin{Bmatrix} \alpha_x \\ \alpha_y \\ \alpha_{xy} \end{Bmatrix} (1, \quad z) T dz \quad (6.c)$$

where  $K$  is a shear correction factor.

Following the standard finite element procedure, the generalized displacements in any element are given by:

$$\begin{Bmatrix} u \\ v \\ w \\ \phi_1 \\ \phi_2 \end{Bmatrix} = \sum_{i=1}^N \begin{Bmatrix} u \\ v \\ w \\ \phi_1 \\ \phi_2 \end{Bmatrix}_i \psi_i \quad (7)$$

where  $N$  is the number of nodes in the element and  $\psi_i$  are the interpolation functions.

Substituting Eq. (7) in Eq. (3), the strains can be expressed as:

$$\varepsilon = B_1\Delta \ ; \ \kappa = B_2\Delta \ ; \ \gamma = B_3\Delta \quad (8)$$

The finite element equation is written as:

$$\left[ K^e \right] \{ \Delta^e \} = \{ F^e \} + \{ F_T^e \} \quad (9)$$

where ,

$$\left[ K^e \right] = \iint \left( B_1^T A B_1 + B_1^T B B_2 + B_2^T B B_1 + B_2^T D B_2 + B_3^T S B_3 \right) d(Area)$$

$$\{ \Delta^e \} = \{ \{ u \} \ \{ v \} \ \{ w \} \ \{ \phi_1 \} \ \{ \phi_2 \} \}^T$$

$$\{ F^e \} = \iint \left( B_1^T N + B_2^T M \right) \cdot d(Area)$$

$$\{ F_T^e \} = \iint \left( B_1^T N^T + B_2^T M^T \right) \cdot d(Area)$$

For any given mechanical and temperature loadings, Eq. (9) can be assembled and solved to determine displacements and stresses.

### 3. COMPOSITE FAILURE MODEL

The Tsai-Wu failure criterion is used for failure evaluation of hydrogen composite storage cylinders [14]. Taking 1 as the fiber direction and 2 and 3 as transverse directions, the Tsai-Wu failure criterion can be expressed as:

$$I_F = F_1\sigma_{11} + F_2\sigma_{22} + F_{11}\sigma_{11}^2 + F_{22}\sigma_{22}^2 + F_{44}\sigma_{23}^2 + F_{55}\sigma_{13}^2 + F_{66}\sigma_{12}^2 + 2F_{12}\sigma_{11}\sigma_{22} < 1.0 \quad (10)$$

The coefficients in Eq. (10) are defined as:

$$F_1 = \frac{1}{X_t} + \frac{1}{X_c}, \quad F_2 = \frac{1}{Y_t} + \frac{1}{Y_c}, \quad F_{11} = -\frac{1}{X_t X_c},$$

$$F_{22} = -\frac{1}{Y_t Y_c}, \quad F_{44} = \frac{1}{S_{23}^2}, \quad F_{55} = \frac{1}{S_{13}^2}, \quad F_{66} = \frac{1}{S_{12}^2},$$

$$F_{12} = \frac{1}{2\sigma_{biax}^2} \left[ 1 - \left( \frac{1}{X_t} + \frac{1}{X_c} + \frac{1}{Y_t} + \frac{1}{Y_c} \right) \sigma_{biax} + \left( \frac{1}{X_t X_c} + \frac{1}{Y_t Y_c} \right) \sigma_{biax}^2 \right]$$

or

$$F_{12} = f \sqrt{F_{11} F_{22}} \quad (-1 \leq f \leq 1)$$

where,  $X_t$  and  $X_c$  are tensile and compressive stress strengths along the fiber direction,  $Y_t$  and  $Y_c$  are tensile and compressive stress strengths in the transverse fiber direction,  $S_{23}$ ,  $S_{13}$  and  $S_{12}$  are the maximum shear strengths in corresponding planes,  $\sigma_{biax}$  is the equi-biaxial stress at failure and  $f$  is an experience coefficient.

#### 4. MATERIAL PROPERTIES

Mechanical and thermal properties of fiber reinforced composites vary significantly with temperature. As the carbon/epoxy laminate carries the pressure loading from the hydrogen gas, the effect of temperature on its material properties cannot be ignored. The moduli and thermal expansion coefficients are dependent on temperature. For HFG CU125 carbon/epoxy, the temperature dependent material properties are given by [15]:

$$E_1 = -0.066 T + 128 \text{ (GPa)} \quad (25^\circ\text{C} < T < 140^\circ\text{C})$$

$$E_2 = -0.064 T + 10.67 \text{ (GPa)} \quad (25^\circ\text{C} < T < 140^\circ\text{C})$$

$$G_{12} = -0.034 T + 5.39 \text{ (GPa)} \quad (25^\circ\text{C} < T < 140^\circ\text{C}) \quad (11)$$

$$\nu_{12} = -0.0005 T + 0.44 \quad (25^\circ\text{C} < T < 140^\circ\text{C})$$

$$\alpha_1 = (0.0003 T^2 - 0.04 T + 2.09) \times 10^{-6} \quad (25^\circ\text{C} < T < 140^\circ\text{C})$$

$$\alpha_2 = (0.0041 T^2 - 0.23 T + 32.2) \times 10^{-6} \quad (25^\circ\text{C} < T < 140^\circ\text{C})$$

Furthermore,  $G_{13}$  is taken as  $G_{12}$ , and  $G_{23}$  is assumed as  $0.7G_{12}$ . The ultimate strengths of carbon/epoxy do not change much with this temperature range and are assumed to be constant and are listed in Table 1. The material properties for glass/epoxy are listed in Table 2. The outer most glass/epoxy layer is primarily used for protection of the load bearing carbon/epoxy lamina. Hence temperature dependent material properties are not used for the glass/epoxy layers. Properties of the innermost aluminum liner are listed in Table 3.

## **5. FINITE ELEMENT SIMULATION**

ABAQUS is an integrated and open-ended Finite Element Analysis code, which is widely used by the industry as well as researchers for the flexibility of implementing user defined subroutines and its powerful nonlinear solver. With those features, the user defined problem can be built up by combination of the basic frames provided by the ABAQUS code and user model specialties implementing subroutines. All the modeling features described in this work have been thus implemented in this code. A laminated shell element, based on doubly curved shell theory, accounting for membrane, bending and membrane-bending coupling and transverse shear effects, is suitable for modeling both thin and thick laminated composites. For this purpose, the laminated composite wall of the cylinder is modeled by using a doubly curved 8-node shell element (S8R). In order to estimate the failure pressure of the cylinder, it is necessary to include a failure criterion. Tsai-Wu failure theory is utilized to check and report the ply-by-ply laminate failure by using a user subroutine UVARM. In addition, the temperature dependent material properties are incorporated in the model by using subroutine USDFLD so that, at

each integration point, the material properties are determined by the given temperature. The orientation of each element at every ply is handled by subroutine ORIENT according to the winding pattern. The cylinder is modeled and meshed using the ABAQUS/CAE preprocessor as shown in Figure 3. Due to the symmetry,  $1/8^{\text{th}}$  of the cylinder is considered for the analysis. The comprehensive model is then solved by using the ABAQUS/standard solver with geometric nonlinearity considered.

The dimensions considered in the present cylinder analysis are based on a typical design from the literature [13]. The outer radius of the cylinder is taken as  $R_{out} = 0.25$  m and the inner radius  $R_{in} = 0.22$  m (Figure 1). The pressure bearing carbon/epoxy laminate consists of 24 plies resulting in a composite shell of thickness 28 mm. The protective glass/epoxy layer and liner are 2 mm and 2.5 mm thick respectively. The cylinder is subjected to an internal pressure that gradually increases until failure occurs in the first ply. To manufacture closed cylinders, two types of winding patterns are usually used: hoop and helical/polar windings. The thickness ratio  $R$  (total thickness of helical laminate/total thickness of hoop laminate) affects the failure pressure of the cylinder and a range of 0.1 to 2.0 is studied. The winding angle of laminae also affects the failure pressure of the cylinder and a range of  $10^{\circ}$  to  $30^{\circ}$  for helical winding and  $89^{\circ}$  for hoop winding has been considered based on manufacturing feasibility. The plies in the protection laminate are oriented as  $45^{\circ}$  angle ply.

## 6. NEURAL NETWORK MODEL

A feedforward back-propagation Neural Network (NNk) is used to predict the failure pressure of a hydrogen cylinder. A schematic of the NNk is shown in Figure 4. The relationship of failure pressure and the inputs (thickness ratio  $R$ , temperature inside the cylinder  $T_{in}$ , temperature outside the cylinder  $T_{out}$ , and winding angle  $\theta$ ) is modeled by a two-layer (hidden layer and output layer) network. Each layer consists of a number of processing units, with an activation function, known as neurons. For faster training and robust NNk, inputs are scaled to a desirable range by a designed transfer function  $f_{in}^T$  before entering the input layer. Inputs are passed through weighted connections to the hidden layer and then to the output layer. The output  $P'$  is, finally, scaled back to failure pressure  $P$  by a designed transfer function  $f_{out}^T$ . The number of neurons in the hidden layer and the characterizing weights and biases in the model are determined by training the NNk.

The input transfer function

$$f_{in}^T(I_i) = I_i \cdot a_i + b_i \quad (12)$$

where

$I_i$  are input variables ( $i = 1, 2, 3$  and  $4$  corresponding to  $R, T_{in}, T_{out}$  and  $\theta$  respectively)

$$a_i = \frac{n_{\max} - n_{\min}}{\vec{I}_i^{\max} - \vec{I}_i^{\min}}$$

$$b_i = n_{\min} - \text{Min}\{a_i \cdot \vec{I}_i\}$$

$[n_{\min} \ n_{\max}]$  is the desired scale range and is taken as  $[-1 \ 1]$

and  $\vec{I}_i$  are input training pattern vectors.

Normalized input variables  $I'_i$  are given by

$$I'_i = f_{in}^T(I_i) \quad (13)$$

The activation function in the hidden layer is the Log-sigmoid function

$$f^h(x) = \frac{1}{1 + e^{-x}} \quad (14)$$

The activation function in the output layer is the Pureline function

$$f^o(x) = x \quad (15)$$

The normalized failure pressure  $P'$  is given by [16]

$$P' = \sum_{j=1}^N W_{1j}^o f^h \left( \sum_{i=1}^4 W_{ji}^h I'_i + b_j^h \right) + b^o \quad (16)$$

where

$N$  is number of neurons in the hidden layer

$W_{1j}^o$  are weights in the output layer

$W_{ji}^h$  are weights in the hidden layer

$b^o$  is bias in the output layer

and  $b_j^h$  are biases in the hidden layer

The output transfer function

$$f_{out}^T(I_i) = (P' - b) / a \quad (17)$$

where

$$a = \frac{n_{\max} - n_{\min}}{\vec{P}^{\max} - \vec{P}^{\min}}, \quad i = 1, 2, 3, \text{ and } 4$$

$$b = n_{\min} - \text{Min}\{a_u \cdot \vec{P}\}, \quad i = 1, 2, 3, \text{ and } 4$$

and  $\vec{P}$  is the output training pattern vector.

The final failure pressure  $P$  is given by

$$P = f_{out}^T(P')$$
 (18)

Training consists of providing a set of known input-output pairs (or patterns) to the network. Back-propagation learning process has two passes through the network: a forward calculation pass and an error back-propagation pass. In the forward pass, input patterns broadcast from input layer to output layer in order to generate the actual results of network. During the backward propagation, weights in each node are iteratively adjusted based on the errors using the gradient descent equations. The procedure is repeated until convergence is achieved. In this study, the input-output sets are obtained from simulation results. The model is trained in MATLAB NNk tool box. The fast training Levenberg-Marquardt Algorithm is adopted in the training process.

## 7. RESULTS AND DISCUSSION

Five configurations of helical and hoop laminas shown in Table 4 are investigated in this study. Case studies are conducted on composite cylinders with various thermal loadings and lay-up patterns. Failure pressures as a function of thickness ratio  $R$  under uniform thermal loadings for Cases 1-3 are shown in Figures 5(a-c) respectively. The rate of increase in failure pressure is higher at higher temperatures. This reflects the nonlinearity of thermal expansion coefficients with variation in temperature. For all the three cases considered, the failure pressure increases with increase in temperature. In comparison with Cases 2 and 3, the peak failure pressure is slightly higher than that of Case 1. Similar results are shown in Figures 6(a-c) with gradient thermal loading. In



comparison with the uniform thermal loadings, the peak failure pressure is not evident for some of the inner temperatures considered in figure 5(b). In those cases, all hoop laminae are placed over helical laminae with inner temperature higher than outer temperature. Then thermal strain, arising from thermal expansion, becomes larger in all helical laminae which cause hoop laminae to carry most of the axial loadings. Without helical laminae sustaining major part of the axial loading, the peak pressure then disappears at lower thickness ratio area. With increasing thickness ratio, the axial-load bearing capacity of the hoop laminae increases thus resulting in the rise in failure pressure. This phenomenon cannot be observed in Figures 6(b-c) because the helical and hoop laminae are laid alternatively. From Figures 6(a-c), with inner temperature increasing (from 25°C to 140°C), the failure pressure rises till it reaches the set temperature (50°C) of outside wall, and then starts to decrease. Also it can be observed that the failure pressure decreases as the gradient of the non-uniform temperature increases.

By comparison of Cases 1, 2 and 3, the alternative lay up pattern (in Cases 2 and 3) can result in higher failure pressure than that of non-alternative lay up (in Case 1), when cylinder is experiencing uniform thermal loading and no significant increase is observed in gradient thermal loading. However, in Case 1, the location of peak pressure varies a lot in comparison with that of Cases 2 and 3 under gradient thermal loading. This large variation might bring down the failure pressure at optimum thickness ratio when considering various thermal loadings in design. There is no significant difference that can be observed between Case 2 (constant winding angle in helical laminate) and Case 3 (gradually increased winding angle in helical laminate). To study the effect of helical winding angle pattern on failure pressure, Cases 2, 4 and 5 ( $[\pm 20^\circ/\pm 89^\circ]_6$  ,

$[\pm 10^\circ/\pm 89^\circ]_6$  and  $[\pm 30^\circ/\pm 89^\circ]_6$ ) are compared with different thickness ratios (R) as shown in Figure 7. For the same thickness ratio, higher peak failure pressure is observed for smaller winding angle.

Figure 8 shows the Tsai-Wu failure indicator for each helical and hoop ply in Case 2 for thickness ratio,  $R=0.5$ . Curves 1 and 2 (T25-25 and T140-140 respectively) illustrate the ply failure under uniform thermal loadings while curves 3 and 4 (T25-100 and T100-25 respectively) show the failure under gradient thermal loadings (T25-25 implies  $T_{in}=25^\circ\text{C}$  and  $T_{out}=25^\circ\text{C}$ ). With uniform thermal loading at  $140^\circ\text{C}$ , the curve is observed to be flat, which implies that all the helical and hoop laminae fail simultaneously. However, at uniform thermal loading of  $25^\circ\text{C}$ , the helical laminae tend to fail first. When subjected to non-uniform thermal loading, a large slope is observed in the curves. The inner layers fail first for T25-100 ( $T_{in}=25^\circ\text{C}$  and  $T_{out}=100^\circ\text{C}$ ), while the outer layers fail for T100-25 ( $T_{in}=100^\circ\text{C}$  and  $T_{out}=25^\circ\text{C}$ ). This asynchronous behavior of inner or outer layers during failure must cause a significant drop in maximum failure pressure, assuming that the cylinder fails when any one of the laminae fails.

The network is trained by using the simulation results from Cases 2, 4 and 5 shown in Table 4. There are 12 neurons used in the neural network (NNk) model and the training ratio is set to 0.01. After the network gets converged, the model parameters are obtained and are listed in Tables 5 and 6. The network model is then capable of predicting the failure pressure by providing the network inputs ( $R, T_{in}, T_{out}$  and  $\theta$ ). To evaluate the performance of NNk prediction, six testing cases (shown in Table 7) are studied. The testing data from ABAQUS simulation results, for winding angles not used before ( $15^\circ$  and  $25^\circ$ ), are used to compare the predicted results from the trained neural network. The

performance of the NNk is then illustrated in Figures 9(a-b), and the maximum errors are reported for each case in Table 7. It can be seen that the simulation results are in good agreement with the results predicted by the NNk model. The trained network can, therefore, be used to predict any failure pressure within the trained ranges of temperature, winding angle and thickness ratio.

## **8. CONCLUSIONS**

A doubly curved shell model accounting for transverse shear deformation is used for thermo-mechanical analysis of hydrogen composite storage cylinders. Temperature dependent material properties of the load carrying carbon/epoxy layer and geometric nonlinearity are also considered in the numerical model. Five typical cases have been considered and the analysis is carried out by applying uniform/non-uniform thermal loading and internal pressure loading. The Tsai-Wu failure criterion is employed to predict the failure pressure by checking the failure, layer by layer. Under uniform thermal loading, a temperature increase significantly increases the maximum failure pressure. Contrastively, the non-uniform thermal loading can cause an uneven load distribution and hence decrease the maximum failure pressure. The thickness ratio also plays an important role in determining the maximum failure pressure and should be selected appropriately based on the thermal and mechanical loading conditions. A neural network (NNk) model is developed and used to predict the failure pressures. The performance of the trained neural network is then evaluated by comparing the predicted values with those of testing cases and the results are in good agreement.

## REFERENCES

- [1] N. Takeichia, H. Senoha, T. Yokotab, H. Tsurutab, K. Hamadab, H. Takeshitac, H. Tanakaa, T. Kiyobayashia, T. Takanod and N. Kuriyamaa, "Hybrid Hydrogen Storage Vessel, A Novel High-pressure Hydrogen Storage Vessel Combined with Hydrogen Storage Material," *International Journal of Hydrogen Energy*, Vol. 28, pp. 1121-1129, 2003.
- [2] C. Liang, H. Chen and C. Wang, "Optimum Design of Dome Contour for Filament-wound Composite Pressure Vessels Based on a Shape Factor," *Composite Structures*, Vol. 58, pp. 469-482, 2002.
- [3] V. V. Vasiliev, A. A. Krikanov and A. F. Razin, "New Generation of Filament-wound Composite Pressure Vessels for Commercial Applications," *Composite Structures*, Vol. 62, pp. 449-459, 2003.
- [4] P. Y. Tabakov and E. B. Summers, "Lay-up Optimization of Multilayered Anisotropic Cylinders Based on a 3-D Elasticity Solution," *Computers and Structures*, Vol. 84, pp. 374-384, 2006.
- [5] J. Park, C. Hong, C. Kim and C. Kim, "Analysis of Filament Wound Composite Structures Considering the Change of Winding Angles Through the Thickness Direction," *Composite Structures*, Vol. 55, pp. 63-71, 2002.
- [6] M. Z. Kabir, "Finite Element Analysis of Composite Pressure Vessels with a Load Sharing Metallic Liner," *Composite Structures*, Vol. 49, pp. 247-255, 2000.
- [7] D. L. Gray and D. J. Moser "Finite Element Analysis of a Composite Overwrapped Pressure Vessel," 40<sup>th</sup> AIAA/ASME/SAE/ASEE Joint Propulsion Conference and Exhibit, Fort Lauderdale, FL, AIAA 2004-3506, pp.1-15, July 11-14, 2004.
- [8] I. H. Akcay and I. Kaynak, "Analysis of Multilayered Composite Cylinders under Thermal Loading," *Journal of Reinforced Plastics and Composites*, Vol. 24, pp.1169-1179, 2005.
- [9] O. Sayman, "Analysis of Multi-layered Composite Cylinders under Hygrothermal Loading," *Composites: Part A*, Vol. 36, pp. 923-933, 2005.
- [10] J. M. Schneider, "Gaseous Hydrogen Station Test Apparatus: Verification of Hydrogen Dispenser Performance Utilizing Vehicle Representative Test Cylinders," SAE World Congress & Exhibition, Detroit, MI, pp.1-10, April 2005.

- [11] K. Chandrashekhara and A. Bhimaraddi, "Thermal Stress Analysis of Laminated Doubly Curved Shells using a Shear Flexible Finite Element," *Computers and Structures*, Vol. 52, pp. 1023-1030, 1994.
- [12] K. Chandrashekhara and T. Schroeder, "Nonlinear Impact Analysis of Laminated Cylindrical and Doubly Curved Shells," *Journal of Composite Materials*, Vol. 29, pp. 2160-2179, 1995.
- [13] F. Mitlitsky, A. H. Weisberg and B. Myers, "Vehicular Hydrogen Storage Using Lightweight Tanks," *Proceedings of the U.S. DOE Hydrogen Program Review NREL/CP-570-28890*, 2000.
- [14] S. W. Tsai and E. M. Wu, "A General Theory of Strength for Anisotropic Materials," *Journal of Composite Materials*, Vol. 5, pp. 58-80, 1971.
- [15] K. J. Yoon and J. Kim, "Prediction of Thermal Expansion Properties of Carbon/Epoxy Laminae for Temperature Variation," *Journal of Composite Materials*, Vol.34, pp. 90-100, 2000.
- [16] M. T. Valoor and K. Chandrashekhara, "A Thick Composite Beam Mode for Delamination Prediction by the Use of Neural Networks," *Composite Science and Technology*, Vol.60, pp. 1773-1779, 2000.

## LIST OF TABLES

Table 1 Ultimate strength of carbon/epoxy composite

Table 2 Mechanical and thermal properties of S-glass/epoxy

Table 3 Mechanical and thermal properties of Aluminum Alloy 6061-T6

Table 4 Lay-up configurations for various winding patterns

Table 5 Weights and biases for trained neural network

Table 6 Scale constants for trained neural network

Table 7 Testing cases and maximum error of prediction

## LIST OF FIGURES

Figure 1 Structure scheme of hydrogen storage cylinder

Figure 2 Doubly curved shell and coordinate system

Figure 3 Finite element model of hydrogen cylinder

Figure 4 Feedforward back-propagation Neural Network architecture

Figure 5(a) Uniform thermal loading with  $T_{in}=T_{out}$  (in Case 1)

Figure 5(b) Uniform thermal loading  $T_{in}=T_{out}$  (in Case 2)

Figure 5(c) Uniform thermal loading  $T_{in}=T_{out}$  (in Case 3)

Figure 6(a) Gradient thermal loading with  $T_{out}=50^{\circ}\text{C}$  (in Case 1)

Figure 6(b) Gradient thermal loading with  $T_{out}=50^{\circ}\text{C}$  (in Case 2)

Figure 6(c) Gradient thermal loading with  $T_{out}=50^{\circ}\text{C}$  (in Case 3)

Figure 7 Failure pressure with inside temperature variation ( $T_{out}=25^{\circ}\text{C}$ )

Figure 8 Ply-by-ply failure predictions under various thermal loadings

Figure 9(a) Comparison of failure pressures from NNk and ABAQUS at  $\theta = 15^{\circ}$

Figure 9(b) Comparison of failure pressures from NNk and ABAQUS at  $\theta = 25^{\circ}$

Table 1 Ultimate strength of carbon/epoxy composite

Strength (MPa)	$F_L^t$	$F_L^c$	$F_T^t$	$F_T^c$	$F_{LT}^S$
	1070	1070	40	170	70



Table 2 Mechanical and thermal properties of S-glass/epoxy

$E_1$ (GPa)	$E_2$ (GPa)	$G_{12} = G_{13}$ (GPa)	$G_{23}$ (GPa)	$\nu_{12}$	$\alpha_1$ ( $1/^\circ\text{C}$ )	$\alpha_2$ ( $1/^\circ\text{C}$ )
55	16	7.6	5.0	0.28	$6.3 \times 10^{-6}$	$32 \times 10^{-6}$
Strength (MPa)	$F_L^t$	$F_L^c$	$F_T^t$	$F_T^c$	$F_{LT}^S$	
	1620	690	40	140	60	

Table 3 Mechanical and thermal properties of Aluminum Alloy 6061-T6

Elastic modulus, E	Poisson's ratio, $\nu$	Yield strength, $\sigma_y$	$\alpha$ ( $1/^\circ\text{C}$ )
70 GPa	0.33	455 MPa	$24.3 \times 10^{-6}$

Table 4 Lay-up configurations for various winding patterns

Case No.	Lay-up pattern	Description
1	$[\pm 20^\circ]_{3s} / [\pm 89^\circ]_{3s}$	24 layers with total thickness of 28 mm $T_{in}=[25 \ 50 \ 75 \ 100 \ 120 \ 140] \text{ }^\circ\text{C}$ $T_{out}=[25 \ 50 \ 75 \ 100 \ 120 \ 140] \text{ }^\circ\text{C}$
2	$[\pm 20^\circ / \pm 89^\circ]_6$	
3	$[\pm 10^\circ / \pm 89^\circ / \pm 14^\circ / \pm 89^\circ / \pm 18^\circ / \pm 89^\circ / \pm 22^\circ / \pm 89^\circ / \pm 26^\circ / \pm 89^\circ / \pm 30^\circ / \pm 89^\circ]$	
4	$[\pm 10^\circ / \pm 89^\circ]_6$	
5	$[\pm 30^\circ / \pm 89^\circ]_6$	

Table 5 Weights and biases for trained neural network

j	Weights in hidden layer				Weights in output layer, $W_{1j}^o$	Biases	
	$W_{j1}^h$	$W_{j2}^h$	$W_{j3}^h$	$W_{j4}^h$		$b_j^h$	$b^o$
1	-1.0803	0.1725	1.7439	-0.3099	54.4500	-6.1185	76.65
2	0.3894	-0.2582	0.1213	0.5764	-123.692	3.6584	
3	-0.4838	0.3915	-0.1974	-0.8114	-36.1329	-3.0100	
4	0.0004	-1.4978	3.5075	0.0280	26.9054	-3.3369	
5	-0.0197	-1.8098	3.9087	0.0127	-19.1409	-3.1452	
6	-8.3694	1.6462	-1.4688	0.0064	-0.3018	-7.8153	
7	-0.3793	0.6444	-0.6923	-0.7765	-1.7120	-0.0646	
8	-1.4274	3.7237	11.3865	0.3180	45.0033	-4.3089	
9	-0.4287	11.4817	-10.7445	-0.6810	0.3312	1.5414	
10	11.3451	-0.0102	0.3561	0.8548	0.6626	11.8876	
11	-1.7027	0.2808	1.7533	-0.2670	-46.5796	-6.7410	
12	1.4200	-3.7174	-11.3598	-0.3166	45.1670	4.3021	

Table 6 Scale constants for trained neural network

$i$	$a_i$	$b_i$	$a$	$b$
1	1.05263	-1.10526	0.05090	-1.96068
2	0.01739	-1.43478		
3	0.01739	-1.43478		
4	0.10000	-2.00000		

Table 7 Testing cases and maximum error of prediction

Testing case	Inputs			Max. Error (%)
	T <sub>in</sub> (°C)	T <sub>out</sub> (°C)	θ (Degree)	
1	40	40	15	1.32
2	30	80	15	-1.54
3	130	40	15	1.23
4	40	40	25	1.11
5	30	80	25	-2.40
6	130	40	25	-1.00

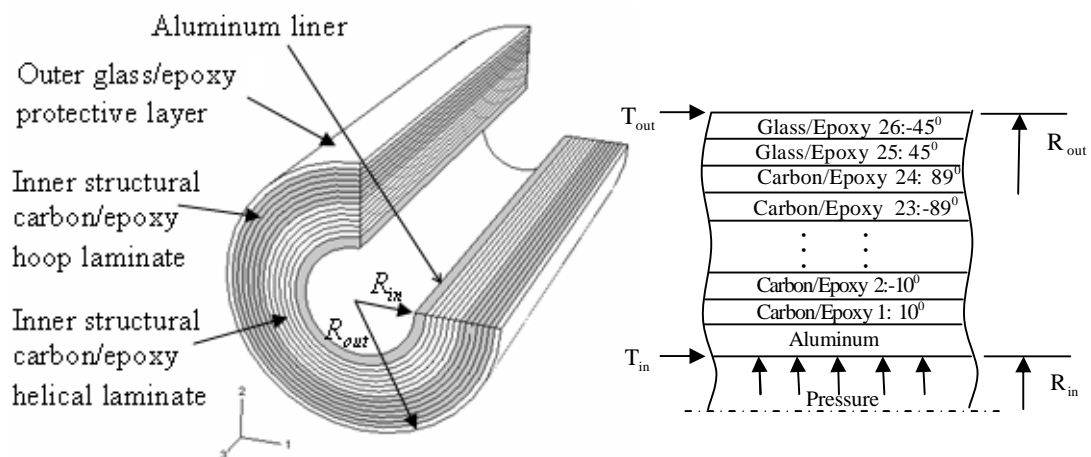


Figure 1 Structure scheme of hydrogen storage cylinder

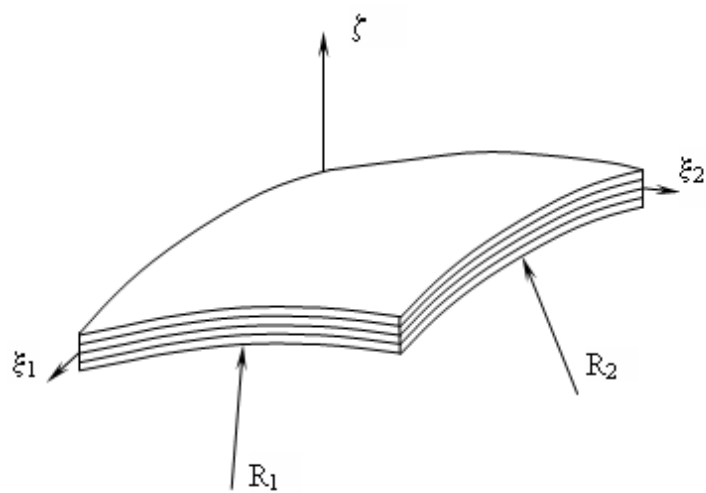


Figure 2 Doubly curved shell and coordinate system



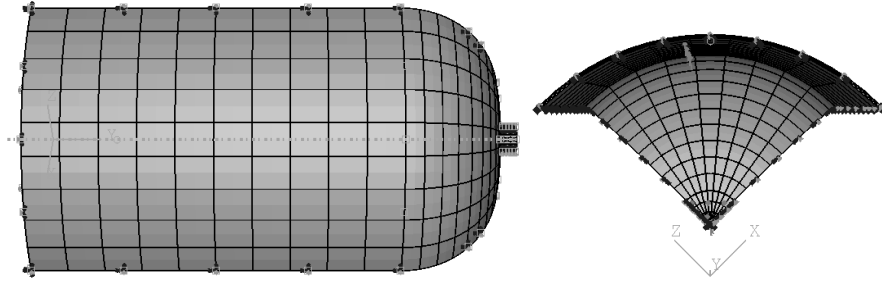


Figure 3 Finite element model of hydrogen cylinder

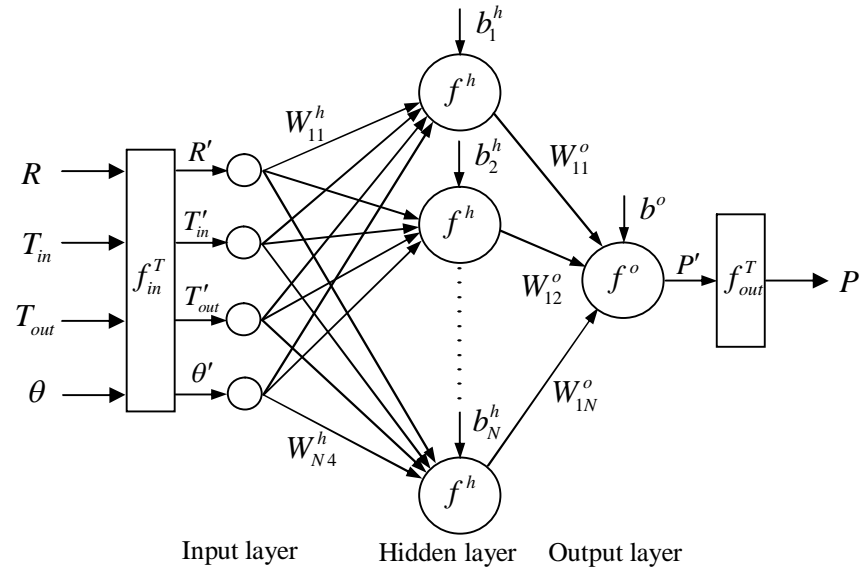


Figure 4 Feedforward back-propagation Neural Network architecture

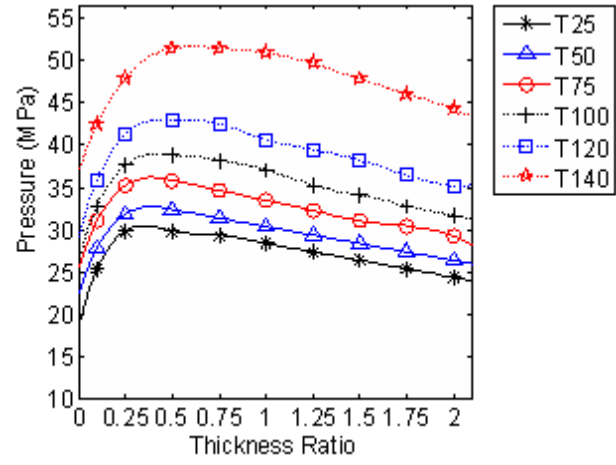


Figure 5(a) Uniform thermal loading with  $T_{in}=T_{out}$  (in Case 1)

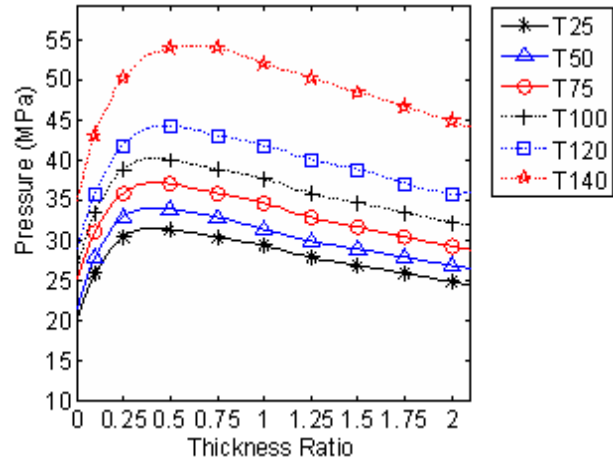


Figure 5(b) Uniform thermal loading  $T_{in}=T_{out}$  (in Case 2)

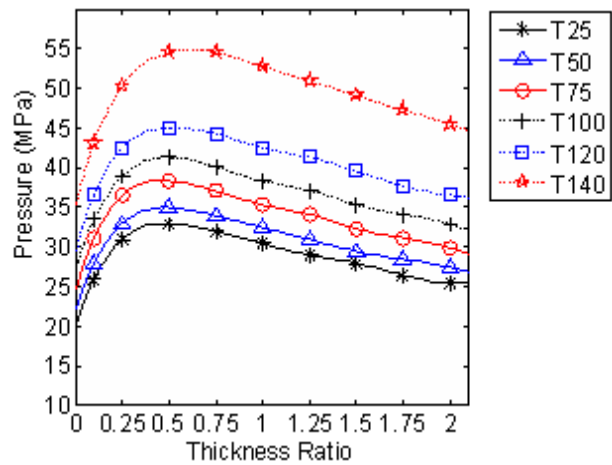


Figure 5(c) Uniform thermal loading  $T_{in}=T_{out}$  (in Case 3)

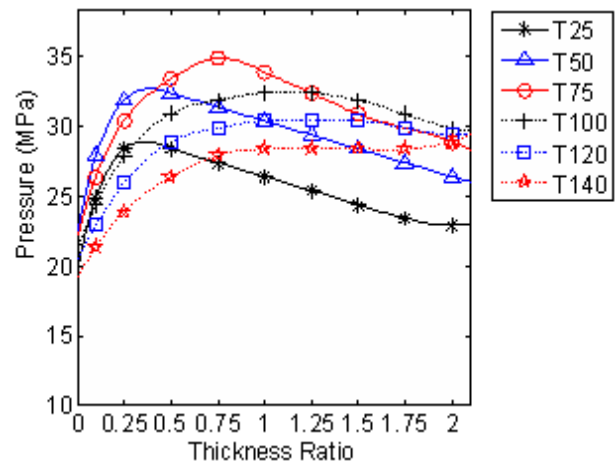


Figure 6(a) Gradient thermal loading with  $T_{out}=50^{\circ}\text{C}$  (in Case 1)

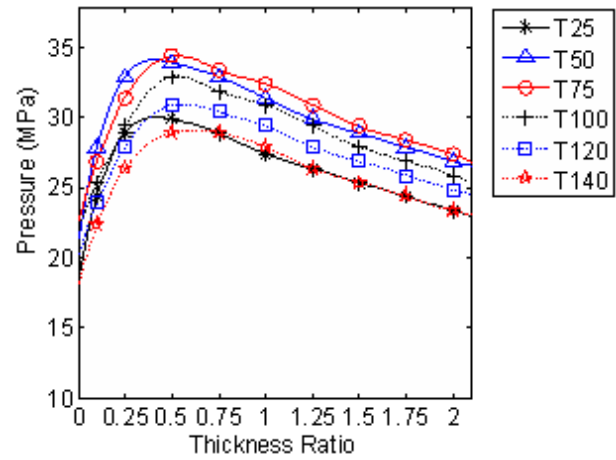


Figure 6(b) Gradient thermal loading with  $T_{out}=50^{\circ}\text{C}$  (in Case 2)

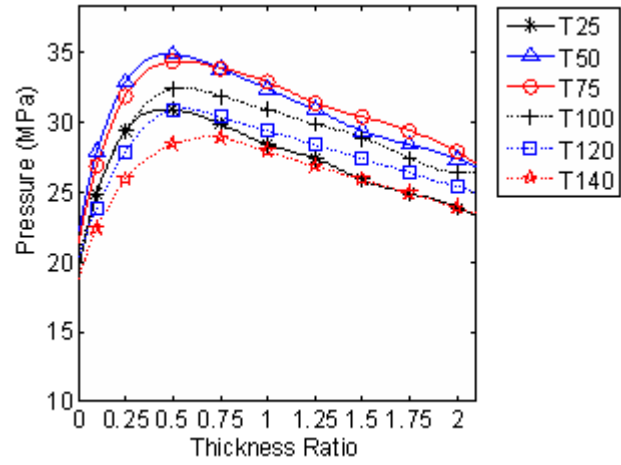


Figure 6(c) Gradient thermal loading with  $T_{out}=50^{\circ}\text{C}$  (in Case 3)



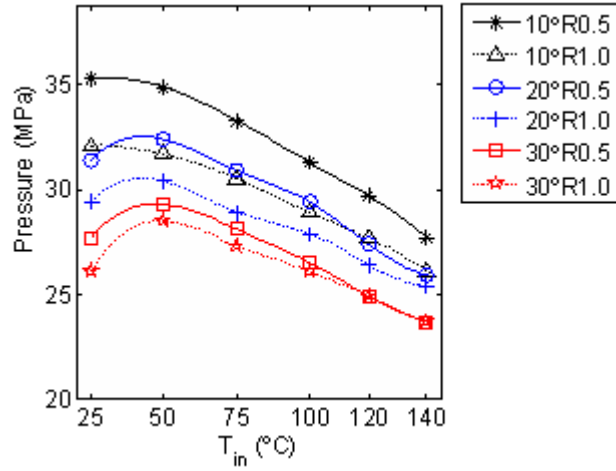


Figure 7 Failure pressure with inside temperature variation ( $T_{out}=25^{\circ}\text{C}$ )

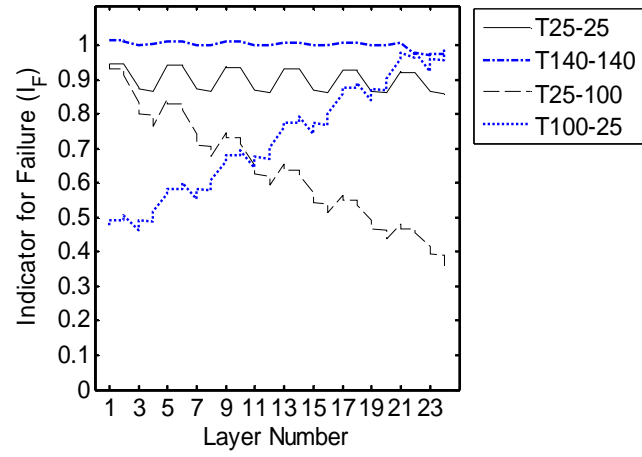


Figure 8 Ply-by-ply failure predictions under various thermal loadings

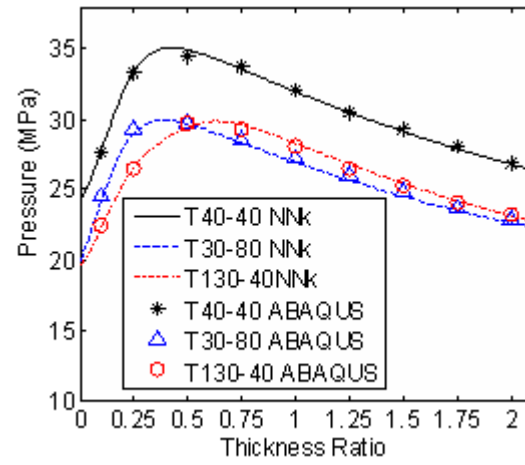


Figure 9(a) Comparison of failure pressures from NNk and ABAQUS at  $\theta = 15^\circ$

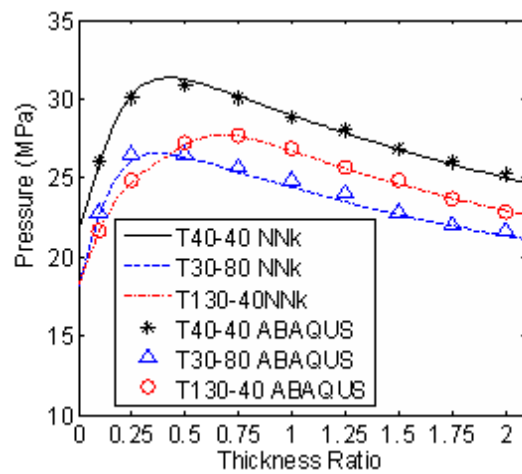


Figure 9(b) Comparison of failure pressures from NNk and ABAQUS at  $\theta = 25^\circ$

**PAPER II:****ANALYSIS OF COMPOSITE HYDROGEN STORAGE CYLINDERS  
SUBJECTED TO LOCALIZED FLAME IMPINGEMENTS****ABSTRACT**

A comprehensive non-linear finite element model is developed for predicting the behavior of composite hydrogen storage cylinders subjected to high pressure and localized flame impingements. The model is formulated in an axi-symmetric coordinate system and incorporates various sub-models to describe the behavior of the composite cylinder under extreme thermo-mechanical loadings. A heat transfer sub-model is employed to predict the temperature evolution of the composite cylinder wall and accounts for heat transport due to decomposition and mass loss. A composite decomposition sub-model described by Arrhenius's law is implemented to predict the residual resin content of the thermal damaged area. A sub-model for material degradation is implemented to account for the loss of mechanical properties. A progressive failure model is adopted to detect various types of mechanical failure. These sub-models are implemented in ABAQUS commercial finite element code using user subroutines. Numerical results are presented for thermal damage, residual properties and the profile of the resin content in the cylinder. The developed model provides a useful tool for safe design and structural assessment of high pressure composite hydrogen storage cylinders.

## 1. INTRODUCTION

High pressure composite cylinders for hydrogen storage are typically made with a high molecular weight polymer or aluminum liner that serves as a hydrogen gas permeation barrier. A filament-wound, carbon/epoxy composite laminate over-wrapped on the outside of the liner provides the desired pressure load bearing capacity. Due to the flammable nature of polymer-reinforced composites, there is a high risk of failure of the composite hydrogen storage cylinder under accidental fire exposure. As the stiffness and strength of composites are temperature dependent, the high pressure (usually 34.5 MPa to 70.0 MPa) in the cylinder can result in catastrophic failure. Therefore, assessment of structural integrity of high pressure composite hydrogen storage cylinders subjected to fire exposure is necessary for safe cylinder design.

Many investigations have been conducted by various researchers [1-4] on the behavior of high pressure composite cylinders under mechanical loadings. Using finite element methods, numerous studies have been performed on high-pressure vessel analysis [5-7]. Compared to pure mechanical loading and pure thermal loading, there have been few studies on the composite cylinders subjected to the combined thermal and mechanical loads [8-9]. However, those models only consider the temperature range before composite decomposition occurs and fall short of providing capability to assess the behavior of cylinders subjected to fire impingement. To study fire effect on composites, different one-dimensional thermal models have been developed to predict the temperature and the residual resin content as a function of time [10-12]. These models account for heat transfer by conduction, resin decomposition, and the cooling effect of volatile products passing through the laminate. Therefore, to characterize the fire

response of high pressure hydrogen composite cylinders, mechanisms of mechanical effect, thermal effect and decomposition have to be considered.

In this paper, a coupled thermo-mechanical finite element model has been developed to simulate composite hydrogen storage cylinders subjected to high pressure and heat flux on the wall surface. The model is formulated in an axi-symmetric coordinate system which accounts for out-of-plane stresses and reduces computational cost dramatically. When the polymer materials are exposed to a sufficiently high temperature (200-300°C), decomposition reactions and thermo-chemical expansion begin to occur and the resin system degrades to form gaseous products and carbonaceous char. In order to incorporate this phenomenon, the thermal model is built to account for gas convection and heat generation due to decomposition in addition to conduction of the composite, convection and radiation of surface. The fire source is modeled as a constant heat flux throughout the simulation. The inner pressure of the cylinder is dependent on the temperature of hydrogen gas which is modeled as a sink temperature. The variation of material properties with temperature is significant for composites, especially at high temperatures. A temperature dependent material model has been developed and implemented. Hashin's theory is used as a progressive failure criterion to predict different types of failure (matrix cracking and fiber breakage). These models are developed and implemented in a commercial finite element code ABAQUS, using user subroutines. A typical high pressure hydrogen composite cylinder is simulated using the developed model and results from the parametric study are reported.

## 2. MODELING OF HIGH PRESSURE COMPOSITE HYDROGEN STORAGE CYLINDERS

A strong sequentially coupled thermal-stress analysis approach is implemented for predicting the behavior of composite hydrogen cylinders subjected to flame impingements and high internal pressure. At each increment, the temperature profile is obtained using the thermal and resin reaction models. The temperature field is then imported to the mechanical model with material damage information from the previous increment. The pressure of the inner cylinder is updated based on the heat absorption of hydrogen gas, which is computed from the temperature profile. The thermal and mechanical models are solved sequentially in each increment. As the wall consists of a large number of laminae, modeling each lamina will cause extraordinary computational cost, especially when thermal and damage models are also incorporated. Hence, a homogenization technique is used to smear several laminae to a sub-laminate as in Figure 1. The equivalent moduli of the sub-laminate are used in the formulation of the finite element model.

### 2.1 Thermal Model

The high temperature will cause resin decomposition of the cylinder composite wall. The decomposition rate of the resin is usually represented by Arrhenius's law and can be expressed as [13]:

$$\frac{\partial \rho}{\partial t} = -A\rho \exp(-E_A / RT) \quad (1)$$

where,

$\rho$  – density



$t$  – time

$T$  – temperature

$A$  – pre-exponential factor

$E_A$  – activation energy

$R$  – gas constant

Material constants  $A$  and  $E_A$  are determined using Differential Scanning Calorimetry. In consideration of the resin reaction, the heat transfer equilibrium equation has to include resin decomposition energy and vaporous migration energy. Since the dimension in the thickness direction is much less than that of hoop and axial directions, the vaporous gas is only assumed to transfer in thickness direction. The axi-symmetric heat diffusion equation can be written as [14]:

$$\rho C_p \frac{\partial T}{\partial t} = \frac{\partial}{\partial r} \left( k_r \frac{\partial T}{\partial r} \right) + \frac{1}{r} \left( k_r \frac{\partial T}{\partial r} \right) + \frac{\partial}{\partial z} \left( k_z \frac{\partial T}{\partial z} \right) + \dot{m}_g C_{pg} \frac{\partial T}{\partial r} + \frac{\partial \rho}{\partial t} (Q - h_{com} - h_g) \quad (2)$$

where,

$C_p$  – specific heat of the composite

$k$  – thermal conductivity

$r$  – displacement through the thickness

$\dot{m}_g$  – gas mass flux

$C_{pg}$  – specific heat of the gas

$Q$  – heat of decomposition

$h_{com}$  – enthalpy of the composite

$h_g$  – enthalpy of hydrogen gas

The mass flow direction of the gas generated in the laminate is towards the hot face of the laminate. The total mass flux of the generated gas at a specific spatial location in the laminate is the sum of the gas mass flux generated from the inner face to this spatial location. The gas mass flux at any spatial location can be calculated as:

$$\dot{m}_g = \int_{t_w}^{r_h} \left( \frac{\partial \rho}{\partial t} \right) dr_h \quad (3)$$

where,

$r_h$  – distance from the hot face

$t_w$  – wall thickness of the composite

## 2.2 Sub-laminate Model

The principle of sub-laminate (Figure 1) homogenization is based on the assumption that the in-plane strains and the interlaminar stresses through the thickness are constant [15-18]. The lamina stress-strain relationship in a global coordinate can be written as:

$$\begin{Bmatrix} \langle \sigma_o \rangle \\ \sigma_i \end{Bmatrix} = \begin{bmatrix} C_{oo} & C_{oi} \\ C'_{oi} & C_{ii} \end{bmatrix} \begin{Bmatrix} \varepsilon_o \\ \langle \varepsilon_i \rangle \end{Bmatrix} \quad (4)$$

where,  $C_{oo}$ ,  $C_{oi}$  and  $C_{ii}$  are sub matrices of global stiffness matrix,  $C'_{oi}$  is the transpose of  $C_{oi}$ ,  $\langle \sigma_o \rangle$  and  $\sigma_i$  are out-of-plane and in-plane stresses respectively,  $\varepsilon_o$  and  $\langle \varepsilon_i \rangle$  are out-of-plane and in-plane strains respectively.  $\langle \rangle$  represents the term is constant through the laminate.

Partially inverting Eq. (4) yields:

$$\begin{Bmatrix} \varepsilon_o \\ \sigma_i \end{Bmatrix} = \begin{bmatrix} C_{oo}^{-1} & -C_{oo}^{-1}C_{oi} \\ C'_{oi}C_{oo}^{-1} & -C'_{oi}C_{oo}^{-1}C_{oi} + C_{ii} \end{bmatrix} \begin{Bmatrix} \langle \sigma_o \rangle \\ \langle \varepsilon_i \rangle \end{Bmatrix} \quad (5)$$

After averaging, Eq. (5) can be expressed as:

$$\begin{Bmatrix} \langle \varepsilon_o \rangle \\ \langle \sigma_i \rangle \end{Bmatrix} = \begin{bmatrix} A & -B \\ B^T & D \end{bmatrix} \begin{Bmatrix} \langle \sigma_o \rangle \\ \langle \varepsilon_i \rangle \end{Bmatrix} \quad (6)$$

$$\text{where, } A = \sum_{k=1}^N \frac{t_k}{t} (C_{oo}^{-1})_k, \quad B = \sum_{k=1}^N \frac{t_k}{t} (C_{oo}^{-1} C_{oi})_k, \quad D = \sum_{k=1}^N \frac{t_k}{t} (-C'_{oi} C_{oo}^{-1} C_{oi} + C_{ii})_k$$

$t_k$  is the thickness of each lamina in the smeared sub-laminate and  $t$  is the total thickness of the smeared sub-laminate.

Partially inverting Eq. (6) yields the equivalent stiffness matrix  $Q_{eq}$  of the sub-laminate as:

$$\begin{Bmatrix} \langle \sigma_o \rangle \\ \langle \sigma_i \rangle \end{Bmatrix} = \begin{bmatrix} A^{-1} & A^{-1}B \\ B^T A^{-1} & B^T A^{-1}B + D \end{bmatrix} \begin{Bmatrix} \langle \varepsilon_o \rangle \\ \langle \varepsilon_i \rangle \end{Bmatrix} \quad (7)$$

The equivalent compliance matrix is given by:

$$[Q_{eq}]^{-1} = \begin{bmatrix} A^{-1} & A^{-1}B \\ B^T A^{-1} & B^T A^{-1}B + D \end{bmatrix}^{-1} = [S_{ij}] \quad (8)$$

Equivalent engineering properties used for the simulation can be obtained from Eq. (8) as:

$$\begin{aligned} E_{11} &= 1/S_{44}, \quad E_{22} = 1/S_{55}, \quad E_{33} = 1/S_{11} \\ G_{12} &= 1/S_{66}, \quad G_{13} = 1/S_{33}, \quad G_{23} = 1/S_{22} \end{aligned} \quad (9)$$

$$v_{12} = -S_{45}/S_{44}, \quad v_{13} = -S_{14}/S_{44}, \quad v_{23} = -S_{15}/S_{55}$$

After the global stresses and strains of the sub-laminates are obtained, the stresses in each lamina are obtained in the global material coordinates as:

$$\begin{aligned} (\sigma_o)_k &= \langle \sigma_o \rangle \\ (\sigma_i)_k &= (B^T)_k \cdot \langle \sigma_o \rangle + (D)_k \cdot \langle \varepsilon_i \rangle \end{aligned} \quad (10)$$

where  $k$  is the  $k^{th}$  lamina of the sub-laminate.

Finally, the stresses in the local material coordinate system can be obtained by standard coordinate transformation.

### 2.3 Formulation of Finite Element Model

Axi-symmetric formulation for transient analysis can be written as:

$$[M^e]\{\ddot{\Delta}^e\} + [K^e]\{\Delta^e\} = \{F^e\} + \{F_T^e\} \quad (11)$$

where  $[M^e] = 2\pi \int_s \rho [N]^T [N] r dS$ ,  $[K^e] = 2\pi \int_s [B]^T [C] [B] r dS$ ,  $\{\Delta^e\} = \{\{u_r\} \{u_\theta\} \{u_z\}\}^T$ ,  $\{F^e\}$  and  $\{F_T^e\}$  are forces due to mechanical and thermal loads respectively. In addition,  $N$  is an interpolation function,  $B$  is the strain displacement function,  $C$  is the elasticity matrix,  $\rho$  is the density, and  $(u_r, u_\theta, u_z)$  are displacement components in the cylindrical coordinate system.

By discretizing Eq. (2), the heat conduction formulation can be expressed as

$$[C_T]\{\dot{T}\} + [K_T]\{T\} = \{H_T\} \quad (12)$$

where

$$[C_T] = \int_V \rho C_p N^T N dV, \quad [K_T] = \int_V N^T \underline{k} N dV, \quad [H_T] = \int_S N^T q_s dS + \int_V N^T q_r dV.$$

where  $\underline{k}$  is thermal conductivity,  $q_s$  is surface heat flux and  $q_r$  is the reaction heat due to resin decomposition and vaporous migration.

The reaction heat  $q_r$  can be expressed as

$$q_r = \dot{m}_g C_{pg} \frac{\Delta T}{\Delta r} + \frac{\Delta \rho}{\Delta t} \left[ Q + (C_{pg} - C_p) \cdot (T - T_\infty) \right] \quad (13)$$

where,  $C_{pg}$  is the specific heat of gas,  $T_\infty$  is ambient temperature and  $Q$  is the heat of decomposition.

Combining Eq. (11) and (12), the sequentially coupled thermal-stress equation can be written as:

$$\begin{bmatrix} M & 0 \\ 0 & 0 \end{bmatrix}^e \begin{Bmatrix} \{\ddot{\Delta}\} \\ 0 \end{Bmatrix}^e + \begin{bmatrix} 0 & 0 \\ 0 & C_T \end{bmatrix}^e \begin{Bmatrix} \{\dot{\Delta}\} \\ \{\dot{T}\} \end{Bmatrix}^e + \begin{bmatrix} K & 0 \\ 0 & K_T \end{bmatrix}^e \begin{Bmatrix} \{\Delta\} \\ \{T\} \end{Bmatrix}^e = \begin{Bmatrix} \{F\} + \{F_T\} \\ \{H_T\} \end{Bmatrix}^e \quad (14)$$

### 3. MATERIAL MODELS

#### 3.1 Temperature Dependent Material Properties

Mechanical and thermal properties of fiber reinforced composites vary significantly with temperature. As the carbon/epoxy laminate carries the pressure loading from the hydrogen gas, the effect of temperature on its material properties cannot be ignored. However, a complete set of temperature dependent properties is not available in the literature. Assumptions and curve fittings are necessary to obtain the material property data based on the limited experimental data that is available. Numerous studies have been done on curve fitting of temperature dependent properties. Gibson et al. [19] shows that a hyperbolic tan (tanh) function is capable of giving an excellent fit to experimental data for material moduli and strength. The equation can be expressed as:

$$P(T) = \left[ \frac{P_U + P_R}{2} - \frac{P_U - P_R}{2} \tanh(k(T - T_g)) \right] C \quad (15)$$

where,  $P(T)$  is the temperature dependent material property,  $P_U$  is the unrelaxed (low temperature) value of that property,  $P_R$  is the relaxed (high temperature) value of that property,  $k$  is a constant describing the width of the distribution,  $T$  is temperature,  $T_g$  is the mechanically determined glass transition temperature and  $C$  is a constant.

Experimental data for carbon/epoxy composite are taken from the literature [20-22]. Moduli are fitted using Eq. (15). The curve fitting parameters are listed in Table 1. The thermal properties of carbon/epoxy are listed in Table 2 and Table 3. Properties for the resin reaction model are listed in Table 4.

The strength of the composite is dependent on temperature and resin content. It has been assumed that the temperature variation of the ultimate longitudinal, transverse and shear strengths of carbon/epoxy follow the same pattern as the longitudinal, transverse and shear moduli respectively and resin content only affects the transverse and shear strengths. The virgin strengths used this investigation are listed in Table 5.

### 3.2 Composite Failure Criteria

As the composite wall of the hydrogen cylinder experiences combined mechanical and thermal loads, a variety of failure types would occur in the process. A progressive failure model is employed in this study to identify the failure types based on failure criterion and predict the safety state of the cylinder. Hashin's failure criterion [23], accounting for four possible modes of ply failure, is used for this purpose.

1. Matrix tensile or shear cracking ( $\sigma_{22} + \sigma_{33} \geq 0$ )

$$I_{mt} = \frac{(\sigma_{22} + \sigma_{33})^2}{(F_T^t)^2} + \frac{\sigma_{12}^2 + \sigma_{13}^2 + \sigma_{23}^2 - \sigma_{22}\sigma_{33}}{(F_{LT}^s)^2} \quad (16)$$

2. Matrix compressive or shear cracking ( $\sigma_{22} + \sigma_{33} < 0$ )

$$I_{mc} = \frac{1}{F_T^c} \left[ \left( \frac{F_T^c}{2(F_{LT}^s)} \right)^2 - 1 \right] (\sigma_{22} + \sigma_{33}) + \frac{(\sigma_{22} + \sigma_{33})^2}{4(F_{LT}^s)^2} + \frac{\sigma_{12}^2 + \sigma_{13}^2 + \sigma_{23}^2 - \sigma_{22}\sigma_{33}}{(F_{LT}^s)^2} \quad (17)$$

3. Fiber tensile fracture ( $\sigma_{11} \geq 0$ )

$$I_{ft} = \left( \frac{\sigma_{11}}{F_L^t} \right)^2 + \frac{1}{(F_{LT}^s)^2} (\sigma_{12}^2 + \sigma_{13}^2) \quad (18)$$

4. Fiber compressive fracture ( $\sigma_{11} < 0$ )

$$I_{fc} = - \left( \frac{\sigma_{11}}{F_L^c} \right) \quad (19)$$

where,  $F_L^t, F_L^c, F_T^t, F_T^c$  and  $F_{LT}^s$  are longitudinal tensile strength, longitudinal compressive strength, transverse tensile strength, transverse compressive strength and shear strength of unidirectional ply respectively.

Once a specific type of failure is identified in the laminate, the reduction in its load-carrying capacity is accounted for, by a reduction in its elastic moduli based on Tan's assumption [24]: (a) When matrix tensile or shear cracking occurs, properties ( $E_{22}, G_{12}, G_{23}$ ) are taken as 0.2 times the original values. (b) When matrix compressive or shear cracking occurs, properties ( $E_{22}, G_{12}, G_{23}$ ) are taken as 0.4 times the original values. (c) When fiber tensile fracture occurs,  $E_{11}$  is taken as 0.07 times the original values. (d) When fiber compressive fracture occurs,  $E_{11}$  is taken as 0.14 times the original values.

### 3.3 Model for Hydrogen Gas

The hydrogen gas in the cylinder absorbs energy and increases the internal pressure. In the present study, the hydrogen gas effect is modeled as a sink whose temperature is updated at each increment based on the amount of heat flux going through the inner cylinder surface. The internal pressure of the cylinder is computed from the state equation of hydrogen. Experimental data for hydrogen gas is taken from the literature [25]. The

pressure and temperature relationship at a constant density of  $23.59 \text{ kg/m}^3$  (when the temperature is  $20^\circ\text{C}$  and the pressure is  $34.5 \text{ MPa}$ ) is curve fitted as shown in Figure 2. The fitted equation is employed to compute cylinder internal pressure.

#### 4. FINITE ELEMENT SIMULATION PROCEDURE

The cylinder dimensions used in the present study are based on the design proposed by Mitlitsky et al. [26] and are summarized in Table 6. An axi-symmetric finite element model is built in ABAQUS as shown in Figure 3. The length of the cylindrical part is taken as  $L_c = 0.3$  for analysis and the dome curve follows a geodesic path. The flame source is modeled as a constant heat flux ( $75 \text{ kW/m}^2$ ) applied on the area with length  $L_s$  throughout the analysis. The radiation, as well as the convection, is also considered at the cylinder outside surface. Pressure is imposed on the inner liner surface. A symmetric boundary condition is applied at the end of the cylinder to reduce the model to half of the cylinder. The model uses SAX8RT element accounting for both deformation and heat transfer. The cylinder wall consists of a inner aluminum liner and six sub-laminates of carbon/epoxy (Figure 4). Each hoop ( $90^\circ$ ) and helical ( $\pm 10^\circ$ ) sub-laminate consists of many laminas.

The implementation procedure of the developed models in ABAQUS is summarized as shown in Figure 5 and the names of interface subroutines are listed in parentheses. At each increment, the material properties are updated (using subroutine USDFLD) based on the information of current temperature, failure type and resin content. The mechanical loading vector is computed from the hydrogen gas model (in the subroutine FILM). The



hydrogen gas model provides the sink temperature from which the internal pressure of the cylinder is computed (from subroutine DLOAD) using the gas state equation. For thermal loading vector, the flame source, resin decomposition, and mass flux of burning gas contribute the heat flux collaboratively (calculated in subroutine HETVAL). The coupled thermo-mechanical equations are then solved to get the global stresses and temperature field. The lamina stresses are retrieved from global stresses and imported into the failure model to compute failure indices. At the next increment, all sub-models (resin sub-model, hydrogen gas sub-model and material strength sub-model) are solved based on the temperature field and failure type from the previous increment. The procedure iterates until the specified time is met. In the present study, this transient analysis is carried out for 1000 seconds.

## **5. RESULTS AND DISCUSSION**

The heat exchange rate between the hydrogen gas and aluminum liner affects the increase in sink temperature (temperature of hydrogen gas) when the cylinder is subjected to flame impingement. In the simulation, the heat exchange rate is represented by a film coefficient ( $H$ ). A parametric study is conducted on  $H$  ranging from 10 to 10,000  $\text{W}/\text{m}^2/^\circ\text{C}$ . The results are shown in Figure 6. The sink temperature increases rapidly with  $H$  at the beginning and flattens out at higher values of  $H$ . At higher  $H$  values, the sink temperature is not sensitive to the heat exchange rate. In real situations, this value can vary over a large range with variation of hydrogen flow rate.  $H$  is taken as 1000  $\text{W}/\text{m}^2/^\circ\text{C}$  for convenience throughout the analysis. Figure 7 plots the internal pressure variation with time for different flame impingement sizes. The non-dimensional  $L$  is defined as

$L=L_s/L_c$  (Figure 3). It can be seen that at the beginning the internal pressure increases very slowly and is much higher after 200 seconds. With increasing size of the flame area, the pressure goes up. For the rest of analysis, results are reported at  $L = 0.1$ .

Figure 8 shows the temperature distributions of the liner internal surface at different times. The temperature of flame impingement center is higher than the adjacent areas. Figure 9 shows the temperature distributions of the composite through the thickness direction at the flame center. The temperature of the outermost sub-laminate 6 increases to 520°C in the first 200 seconds and then continues to go up very slowly during the rest of the time. The innermost sub-laminate 1 increases slowly during the entire flame impingement process. Figure 10 shows the residual resin content in the composite through the thickness at the flame center. In the outermost sub-laminate 6, resin is depleted totally in the first 100 seconds and in the innermost sub-laminate 1, the resin content keeps almost constant throughout the entire process.

Stress distributions through the composite thickness at the end of the simulation time are reported in Figures 11 and 12. An uneven stress ( $S_{11}$ ) distribution is observed in the fiber direction for hoop sub-laminates. This can result in the breakage of fibers in the inner hoop layers. The stresses in the transverse direction ( $S_{22}$ ) and thickness direction ( $S_{33}$ ) are plotted in Figure 12. The shear stresses are not reported as they are negligibly small.

Failures due to fiber fracture, matrix cracking and resin depletion are presented in Figure 13 (a-c). A higher fiber fracture index is observed for the inner layer. This is because the fibers of outer layers cannot bear much mechanical load as the resin is either depleted or softened due to the high temperature. Matrix cracking is observed at the inner

half of the composite wall. However, the matrix failure index is very low at the outermost layers, since there is not much matrix (resin) left. Hence, no significant mechanical loading can be carried in this part. This can be observed in Figure 13(c).

## 6. CONCLUSIONS

A comprehensive finite element model has been developed to analyze composite hydrogen storage cylinders subjected to high pressure and flame impingements. The model considers the resin reaction, heat exchange between the hydrogen gas and liner, and the progressive failure process. A sub-laminate model has been developed to reduce the computational time. A temperature dependent material model and the failure models have been developed and implemented to accurately predict various types of failure for the hydrogen storage cylinder. All the models are formulated in an axi-symmetric coordinate system and implemented in ABAQUS through user subroutines. Analysis of a typical high pressure composite hydrogen cylinder under fire exposure is conducted by using the developed model. Parametric studies are done on heat exchange rate (between hydrogen gas and liner) and the size of flame source. Stresses, temperature profile and failure types are reported. The developed model can be used to accommodate various types of thermal and mechanical loadings, lamina stacking sequence, and lamina thickness to establish safe working conditions and design limits for hydrogen storage cylinders. In addition, this simulation process can be used for both type III and type IV hydrogen cylinders, as both have a similar structure except for the type of liner being used.

## REFERENCES

- [1] C. Liang, H. Chen and C. Wang, "Optimum Design of Dome Contour for Filament-wound Composite Pressure Vessels Based on a Shape Factor," *Composite Structures*, Vol. 58, pp. 469-482, 2002.
- [2] V. V. Vasiliev, A. A. Krikanov and A. F. Razin, "New Generation of Filament-wound Composite Pressure Vessels for Commercial Applications," *Composite Structures*, Vol. 62, pp. 449-459, 2003.
- [3] P. Y. Tabakov and E. B. Summers, "Lay-up Optimization of Multilayered Anisotropic Cylinders Based on a 3-D Elasticity Solution," *Computers and Structures*, Vol. 84, pp. 374-384, 2006.
- [4] D. Chapelle and D. Perreux, "Optimal Design of a Type 3 Hydrogen Vessel: Part I- Analytic Modeling of the Cylindrical Section," *International Journal of Hydrogen Energy*, Vol.31, pp. 627-638, 2006.
- [5] J. Park, C. Hong and C. Kim, "Analysis of Filament Wound Composite Structures Considering the Change of Winding Angles through the Thickness Direction," *Composite Structures*, Vol. 55, pp. 63-71, 2002.
- [6] M. Z. Kabir, "Finite Element Analysis of Composite Pressure Vessels with a Load Sharing Metallic Liner," *Composite Structures*, Vol. 49, pp. 247-255, 2000.
- [7] D. L. Gray and D. J. Moser "Finite Element Analysis of a Composite Overwrapped Pressure Vessel," 40<sup>th</sup> AIAA/ASME/SAE/ASEE Joint Propulsion Conference and Exhibit, Fort Lauderdale, FL, AIAA 2004-3506, pp. 1-15, July 11-14, 2004.
- [8] I. H. Akcay and I. Kaynak, "Analysis of Multilayered Composite Cylinders under Thermal Loading," *Journal of Reinforced Plastics and Composites*, Vol. 24, pp. 1169-1179, 2005.
- [9] O. Sayman, "Analysis of Multi-layered Composite Cylinders under Hygrothermal Loading," *Composites: Part A*, Vol. 36, pp. 923-933, 2005.
- [10] J. B. Henderson, J. A. Wiebelt and M. R. Tant, "A Model for the Thermal Response of Polymer Composite Materials with Experimental Verification," *Journal of Composite Materials*, Vol. 19, pp. 579-595, 1985.
- [11] J. B. Henderson and T. E. Wiecek, "A Mathematical Model to Predict the Thermal Response of Decomposing, Expanding Polymer Composites," *Journal of Composite Materials*, Vol. 21, pp. 373-393, 1987.
- [12] A. G. Gibson, P. N. H. Wright and Y-S. Wu, "The Integrity of Polymer Composites during and after Fire," *Journal of Composite Materials*, Vol. 38, pp. 1283-1307, 2004.
- [13] K. J. Laidler, "Theories of Chemical Reactions Rates," McGraw-Hill: New York, 1969.
- [14] J. Lua, J. O'Brien, C. T. Key, Y. Wu and B. Y. Lattimer, "A Temperature and Mass Dependent Thermal Model for Fire Response Prediction of Marine Composites,"

- Composites Part A: Applied Science and Manufacturing, Vol. 37, pp.1024-1039, 2006.
- [15] P. C. Chou and J. Carleone, "Elastic Constants of Layered Media," *Journal of Composite Materials*, Vol. 6, pp. 80-93, 1972.
- [16] C. T. Sun and S. Li, "Three-dimensional Effective Elastic Constants for Thick Laminates," *Journal of Composite Materials*, Vol. 22, pp. 629-639, 1988.
- [17] H. Chen and S. W. Tsai, "Three-dimensional Effective Moduli of Symmetric Laminates," *Journal of Composite Materials*, Vol. 30, pp. 906-916, 1996.
- [18] J. Whitcomb and J. Noh, "Concise Derivation of Formulas for 3D Sublaminar Homogenization," *Journal of Composite Materials*, Vol. 34, pp. 522-535, 2000.
- [19] A. G. Gibson, Y.-S. Wu, J. T. Evans and A. P. Mouritz, "Laminate Theory Analysis of Composites under Load in Fire," *Journal of Composite Materials*, Vol. 40, pp. 639-658, 2006.
- [20] K. J. Yoon and J. Kim, "Prediction of Thermal Expansion Properties of Carbon/Epoxy Laminates for Temperature Variation," *Journal of Composite Materials*, Vol. 34, pp. 90-100, 2000.
- [21] G. Kalogiannakis, D. V. Hemelrijck and G. V. Assche, "Measurements of Thermal Properties of Carbon/Epoxy and Glass/Epoxy using Modulated Temperature Differential Scanning Calorimetry," *Journal of Composite Materials*, Vol. 38, pp. 163-175, 2004.
- [22] G. Liang, A. Garg, K. Chandrashekhara, V. Flanigan and S. Kapila, "Cure Characterization of Pultruded Soy-based Composites," *Journal of Reinforced Plastics and Composites*, Vol. 24, pp. 1509-1520, 2005.
- [23] Z. Hashin, "Failure Criteria for Unidirectional Fiber Composites," *Journal of Applied Mechanics*, Vol. 47, pp. 329-334, 1980.
- [24] S. C. Tan, "A Progressive Failure Model for Composite Laminates Containing Openings," *Journal Composite Materials*, Vol. 25, pp. 556-577, 1991.
- [25] W. E. Deming and L. E. Shupe, "Some Physical Properties of Compressed Gases, III. Hydrogen," *Physical Review*, Vol. 40, pp. 848-859, 1932.
- [26] F. Mitlitsky, A. H. Weisberg, and B. Myers, "Vehicular Hydrogen Storage using Lightweight Tanks," *Proceedings of the 2000 U.S.DOE Hydrogen Program Review*, NREL/CP-570-28890, pp. 1-82, 2000.

**LIST OF TABLES**

Table 1 Curve fitting parameters for transverse and shear modulus

Table 2 Thermal expansion coefficients of carbon/epoxy

Table 3 Specific heat and thermal conductivity of carbon/epoxy

Table 4 Parameters for resin reaction model

Table 5 Strength of carbon/epoxy

Table 6 Design parameters for the cylinder

## LIST OF FIGURES

- Figure 1 Schematic of hydrogen cylinder
- Figure 2 Curve fitting for hydrogen gas state equation at constant density
- Figure 3 Finite element model of the cylinder
- Figure 4 Stacking sequence of the cylinder wall
- Figure 5 Finite element implementation schemes
- Figure 6 Variation of sink temperature with film coefficient
- Figure 7 Internal pressure variation with time for various flame area sizes
- Figure 8 Temperature distributions along the length at inner surface of the aluminum liner
- Figure 9 Temperature distributions through composite thickness
- Figure 10 Residual resin content through the thickness
- Figure 11 Stress ( $S_{11}$ ) distribution through the thickness
- Figure 12 Stress ( $S_{22}$ ,  $S_{33}$ ) distribution through the thickness
- Figure 13(a) Fiber fracture index ( $I_{mt}$ ) contour around heat source
- Figure 13(b) Matrix cracking index ( $I_{ft}$ ) contour around heat source
- Figure 13(c) Density index ( $\rho/\rho_0$ ) contour around heat source

Table 1 Curve fitting parameters for transverse and shear modulus

	Longitudinal modulus	Transverse modulus	Shear modulus
$P_U$ (GPa)	133.35	9.135	4.515
$P_R$ (GPa)	111	0.1	0.045
K	0.0064	0.022	0.02
C	1	1	1
$T_g$ ( $^{\circ}$ C)	100	100	100



Table 2 Thermal expansion coefficients of carbon/epoxy

Temperature (°C)	$\alpha_1(1 \times 10^{-6} / ^\circ\text{C})$	$\alpha_2(1 \times 10^{-6} / ^\circ\text{C})$
20	1.47	29.2
40	0.97	29.5
60	0.77	33.2
80	0.81	40.0
100	1.09	50.2
120	1.61	63.6
140	2.37	80.4
350	9.03	238.0

Table 3 Specific heat and thermal conductivity of carbon/epoxy

Specific heat	
Temperature (°C)	Cp (kJ/kg/°C)
0	0.8
20	0.86
70	1.08
95	1.28
120	1.4
170	1.5
260	1.67
350	1.84
Thermal conductivity (W/m/°C)	
$K_{11} = 6.5$	
$K_{22} = 0.65$	
$K_{33} = 0.65$	

Table 4 Parameters for resin reaction model

Properties	Values
Pre-exponential factor, A(1/sec)	500.0
Activation energy, $E_A$ (kJ/kg-mole)	$6.05 \times 10^4$
Gas constant, R (kJ/kg-mole/ $^{\circ}$ C)	8.314
Specific heat of gas, $C_{pg}$ (J/kg/ $^{\circ}$ C)	2386.5
Specific heat of composite, $C_p$ (J/kg/ $^{\circ}$ C)	1066.0
Heat of decomposition, Q (J/kg)	$3.5 \times 10^5$

Table 5 Strength of carbon/epoxy

Strengths (MPa)	$F_L^t$	$F_L^c$	$F_T^t$	$F_T^c$	$F_{LT}^S$
	2463	1070	40	170	60

Table 6 Design parameters for the cylinder

Parameters	Values
Outside diameter (m)	0.462
Liner thickness (mm)	2.54
Composite thickness (mm)	11.3
Thickness ratio (helical/hoop)	0.65
Stress ratio (helical/hoop)	0.8
Operation pressure (MPa)	34.5
Factor of safety	2.25

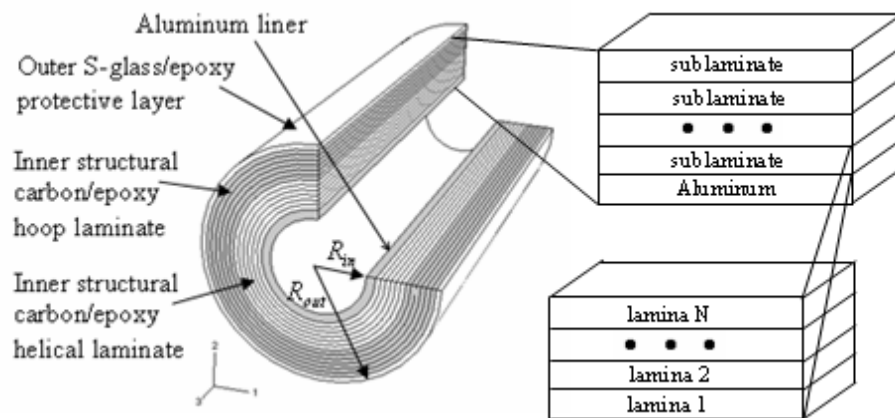


Figure 1 Schematic of hydrogen cylinder

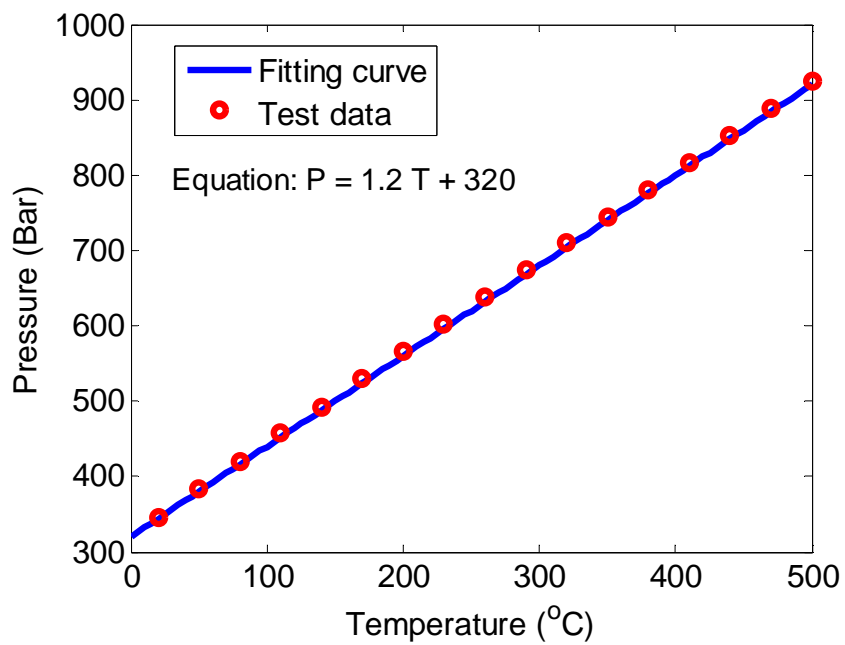


Figure 2 Curve fitting for hydrogen gas state equation at constant density

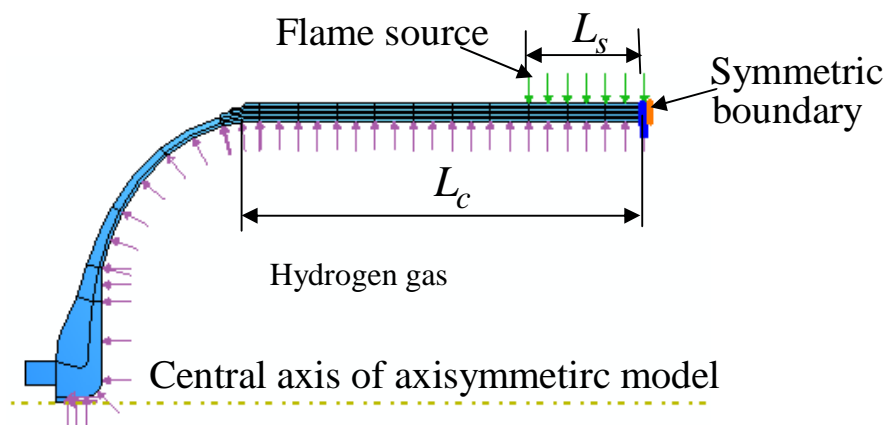


Figure 3 Finite element model of the cylinder



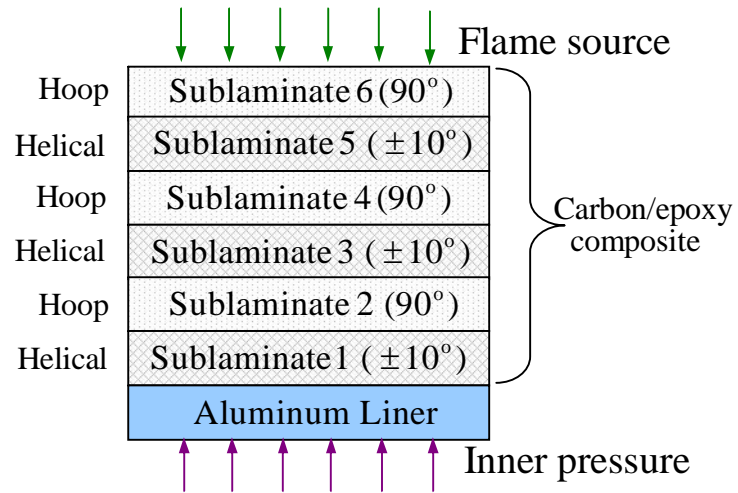


Figure 4 Stacking sequence of the cylinder wall

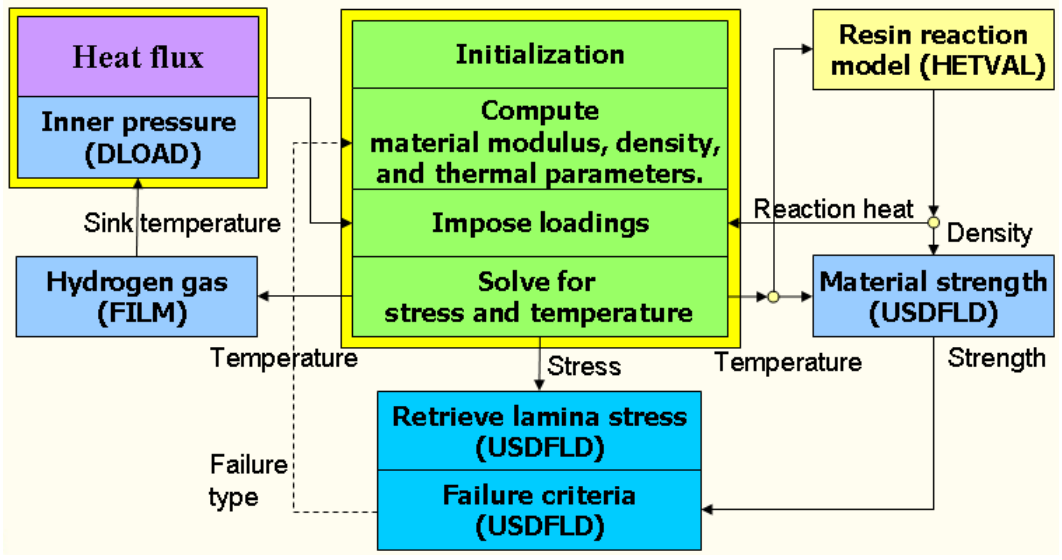


Figure 5 Finite element implementation schemes

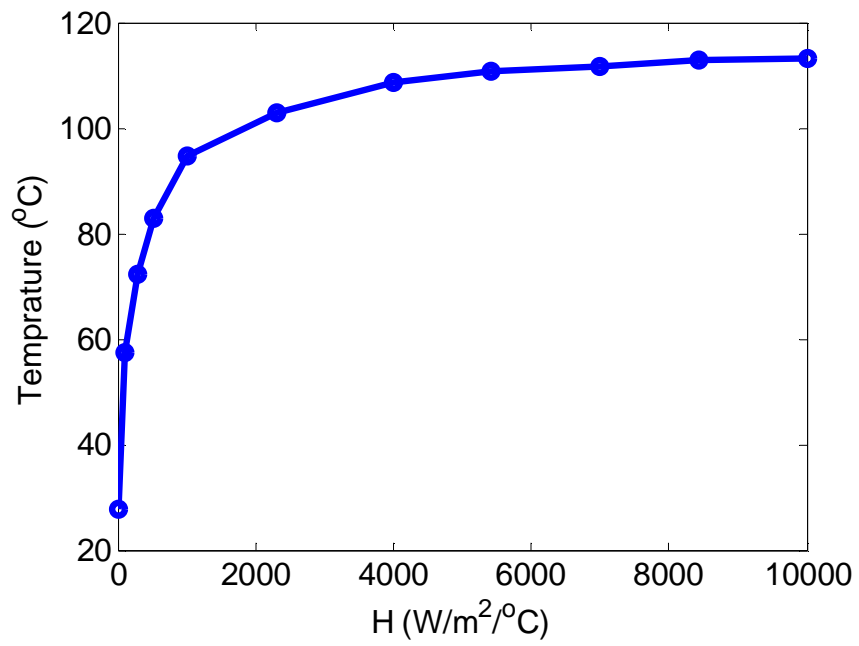


Figure 6 Variation of sink temperature with film coefficient

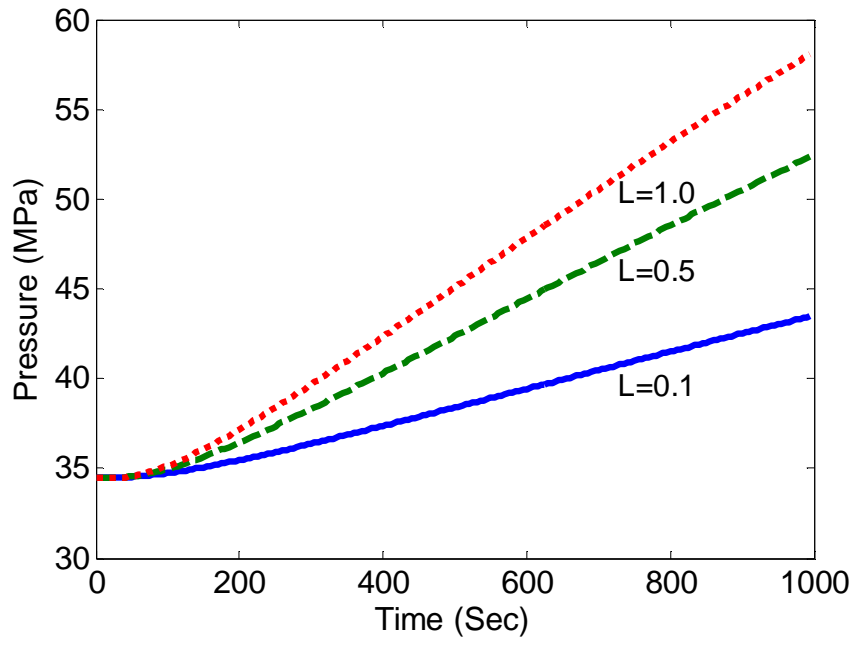


Figure 7 Internal pressure variation with time for various flame area sizes

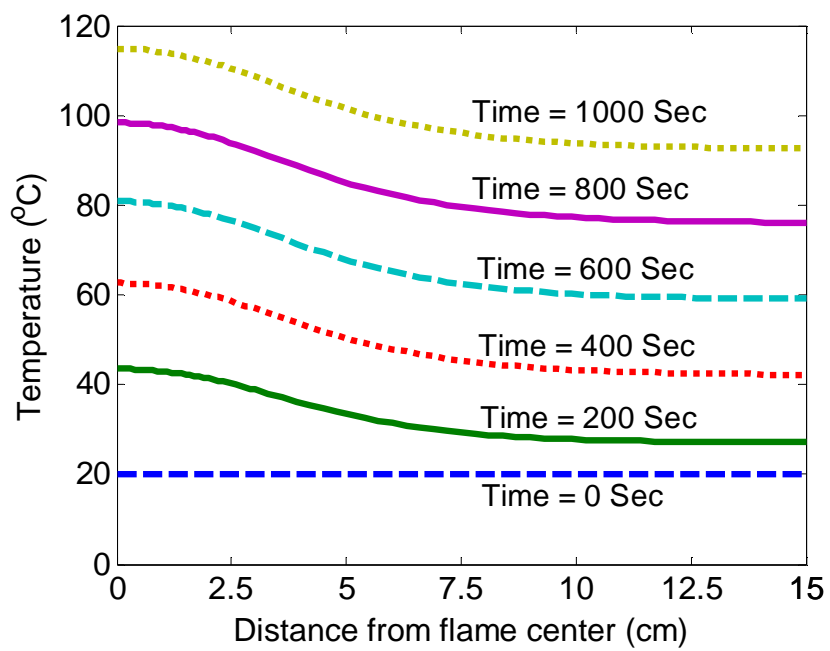


Figure 8 Temperature distributions along the length at inner surface of the aluminum liner

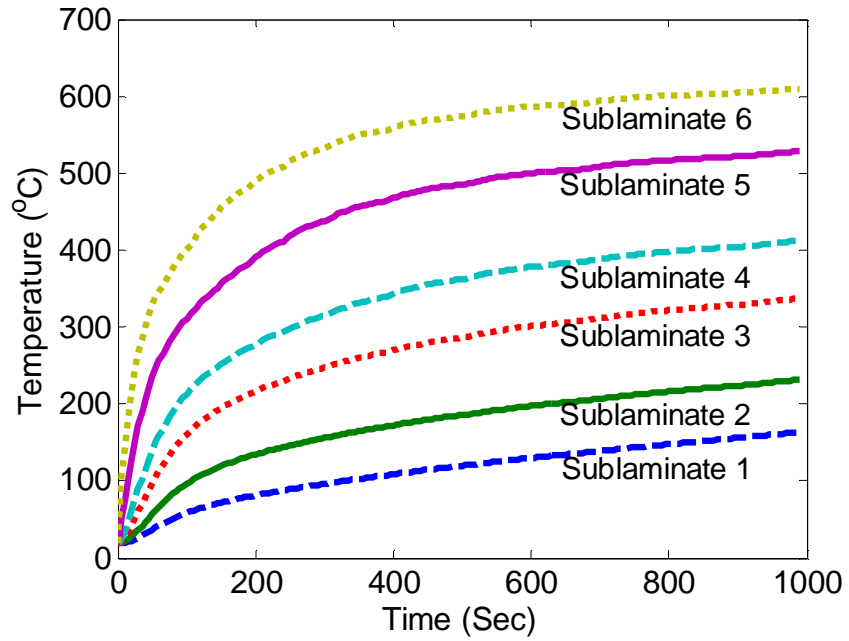


Figure 9 Temperature distributions through composite thickness

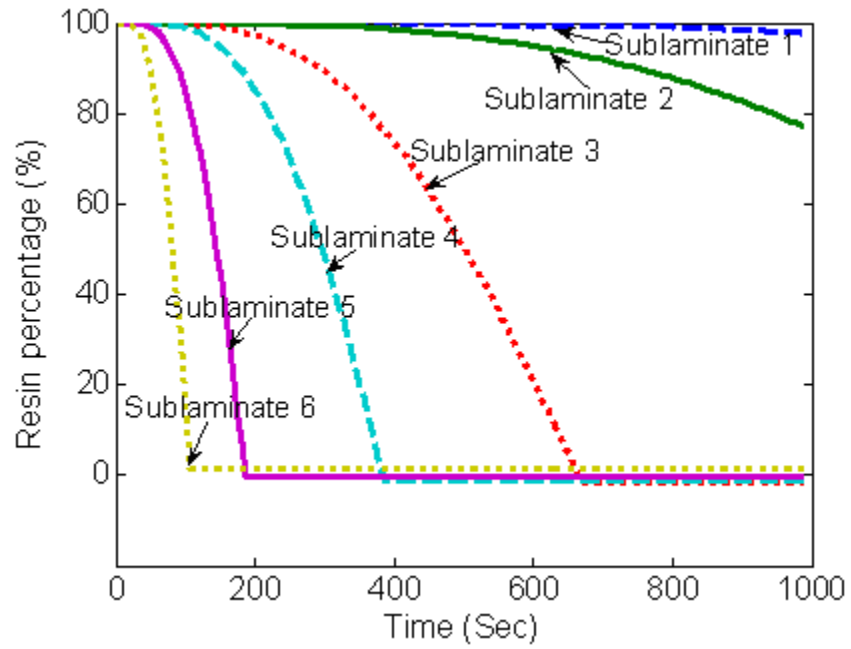


Figure 10 Residual resin content through the thickness

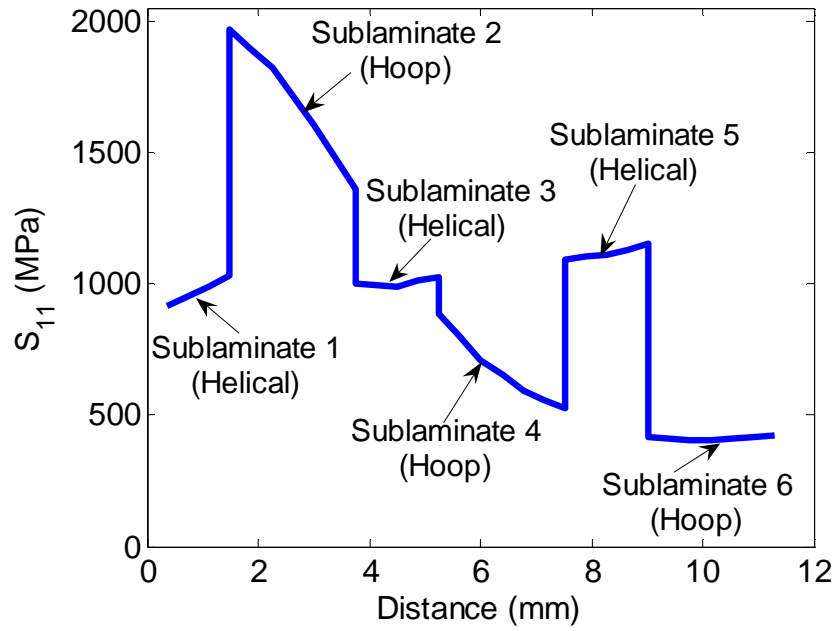


Figure 11 Stress ( $S_{11}$ ) distribution through the thickness



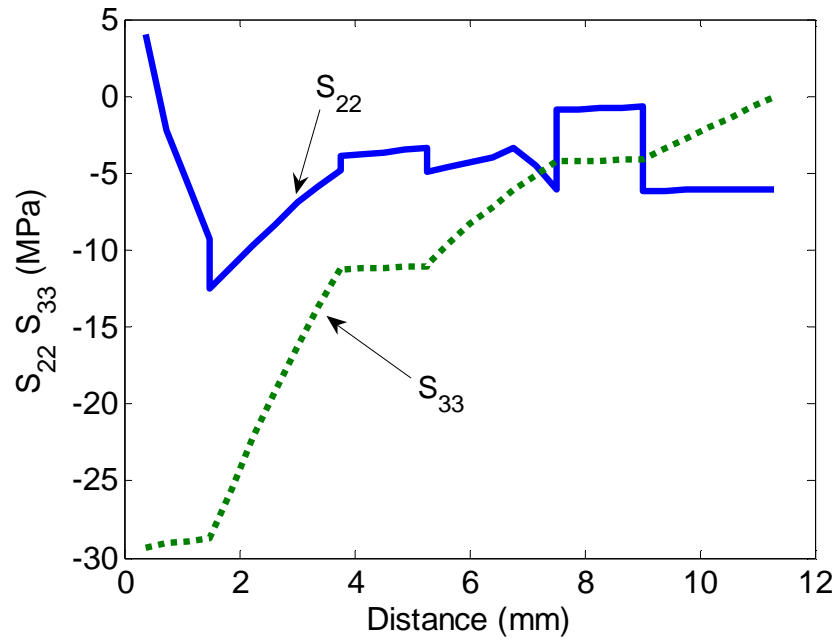


Figure 12 Stress ( $S_{22}$ ,  $S_{33}$ ) distribution through the thickness

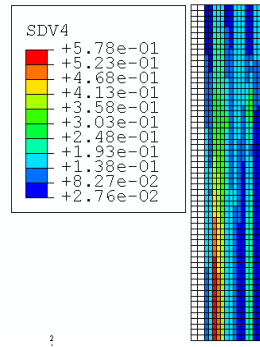


Figure 13(a) Fiber fracture index ( $I_{mt}$ ) contour around heat source

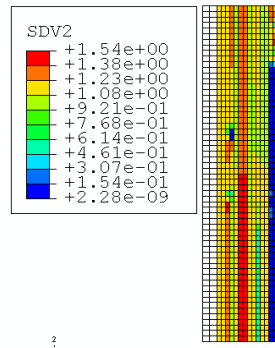


Figure 13(b) Matrix cracking index ( $I_{ft}$ ) contour around heat source

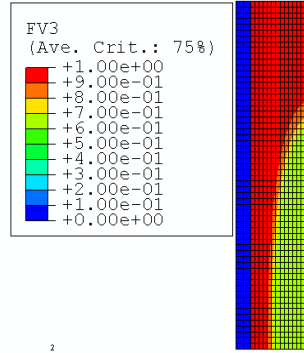


Figure 13(c) Density index ( $\rho/\rho_0$ ) contour around heat source

**PAPER III:****FRACTURE ANALYSIS OF HYDROGEN STORAGE COMPOSITE  
CYLINDERS WITH LINER CRACK ACCOUNTING FOR AUTOFRETTAGE  
EFFECT****ABSTRACT**

An understanding of fracture behavior is crucial to the safe installation and operation of high pressure composite cylinders for hydrogen storage. This work has developed a comprehensive finite element model to investigate axial surface flaws in cylinder liners using the fracture mechanics and a global-local finite element technique. Since the autofrettage process has a strong influence on cylinder fracture behavior, it is also considered in this analysis. The simulation process is broken down into three steps in order to precisely extract fracture parameters and incorporate the autofrettage effect. In the first step, the global model performs the autofrettage simulation to study the residual stress with consideration of both material hardening and the Bauschinger effect. In the second step, the global model uses residual stress to compute displacement for the local model. Finally, in the third step, the local model extracts the values of stress intensity factor (K) and J-integral. Comparison is conducted on the fracture parameters with various autofrettage levels and crack shapes. The vicinity of crack front is also studied by the size and shape of the plastic zone, and the validity of stress intensity factor (K) and J-integral dominances is examined.

## 1. INTRODUCTION

High pressure composite cylinders have gained the intensive attention of the automotive industry as hydrogen storage media for hydrogen vehicles [1]. These cylinders are typically made of an aluminum liner wrapped with carbon/epoxy composites. The composite wrap is designed to withstand high pressure loading (5,000-10,000Psi) of compressed hydrogen gas while maintaining a light weight through the use of high strength, low density composite materials. The aluminum liner serves as the hydrogen barrier layer since the material provides a perfect resistance for hydrogen permeation [2]. However, this advantage is undermined by manufacturing defects that lead to the development of cracks in the liner. Due to the driving force from the internal pressure, continuous propagation of cracks will lead to serious leakage and eventual failure of the cylinder. The fracture behavior of the aluminum liner, therefore, is a key factor affecting the operational safety and design life expectancy of the cylinder.

Fracture analysis of composite cylinders stems from studies of various pipes and vessels. Since surface flaws commonly occur in these products and propagate during service, they are involved in most studies. In general, surface flaws are represented in the analysis by semi-elliptical shapes. Fracture parameters such as the stress intensity factor (K) and the J-integral, which determine the crack criteria and cause of failure, are computed along the front of a semi-elliptical crack [3,4]. Due to their geometric complexity, only a few analytical solutions have been proposed to determine those parameters with low computational cost [5-7]. Since those methods rely on simplified assumptions about material models and the stress field near the crack tip, they are suitable for a simple geometry and linear analysis.

The finite element (FE) method provides a more general and flexible tool for evaluation of both stress intensity factor (K) and J-integral, and results have been widely reported in the literature. Rice and Levy [8] introduced a line-spring element model to compute K, and that work was expanded by Lee and Parks [9] to evaluation of J-integral and T stress. Raju et al. [10] computed K for internal and external surface cracks in cylindrical vessels using a 3D continuum element. Kim et al. [11] analyzed internal axial surface cracks in cylinders considering various geometric ratios and material plasticity. Diamantoudis and Labeas [12] modeled the cracks at various locations on a pressure vessel using a global-local FE technique. Guerrero et al. [13] improved a pressure vessel design based on a detailed FE fracture analysis. Su et al. [14-16] performed fracture analysis on a series of compressed natural gas cylinders. Based on previous studies, most research has addressed to metallic cylinders, and few studies have focused on metallic liners with a composite wrap in the hoop direction. Still less work has studied the full composite-wrapped cylinder with consideration of the autofrettage effect.

Autofrettage is a metal fabrication technique, commonly used in increasing durability of high-pressure cylinders, cannon barrels and diesel engines. In this technique, the cylindrical product is subjected to enormous pressure, causing internal portions of the part to yield and resulting in internal compressive residual stresses to enhance product fracture performance. Since autofrettage has strong influence on cylinder fracture behavior, this paper investigates liner cracks of high pressure composite cylinders for hydrogen storage considering autofrettage effect using fracture mechanics and a global-local FE technique. The global-local FE model has been developed in a commercial FE code, ABAQUS. The autofrettage effect is studied in the global model. The local model,

which is driven by the results of the global model, analyzes the crack in detail to ensure accurate computation of fracture parameters. Results for both  $K$  and the  $J$ -integral are reported for four autofrettage levels along the crack front. The effect of crack size is also examined using cracks with various depth/thickness and depth/width ratios. In addition, since the stress field in the vicinity of the crack tip determines the validity of fracture parameter characterization, which is crucial for design parameter selection, the plastic zone around the crack front is studied.

## **2. METHODOLOGY**

A schematic of a hydrogen composite cylinder with an inner surface flaw is shown in Figure 1. The inner liner is made of aluminum alloy that serves as a hydrogen gas permeation barrier. Filament-wound carbon/epoxy composite laminates wrap the liner in both the hoop and the helical directions. These laminates provide the desired pressure load bearing capacity. Due to the inner hydrogen pressure, cracks develop as a result of manufacturing defects and propagate in the liner wall during service. In order to restrain crack propagation, the autofrettage process is conducted before the cylinder enters service by introducing proper compressive stresses in the liner [17]. Stress intensity factor ( $K$ ) and the  $J$ -integral provide a means to study the fracture performance of the cylinder according to the various deformation states.

### **2.1 The Autofrettage Effect on Hydrogen Storage Composite Cylinders**

The fracture resistance of composite hydrogen cylinders can be improved by the autofrettage process, in which the cylinder is pressurized to a specified proof pressure to produce a desired compressive stress level in the liner. Figure 2 illustrates the process



with stress-strain and load versus time curves. The autofrettage process is conducted in the first cycle pressure loading (0→2→4) as shown in Figure 2(b). Afterwards, the pressure will cyclically remain between zero and operating pressure ( $4 \leftrightarrow 4'$ ) in service.

During autofrettage (0→2), the composite wrap responds linearly in an elastic state, as represented by the dotted line from 0 to A in Figure 2(a). At the same time, the liner undergoes elasto-plastic deformation represented by the solid curve (0→1→2). Large plastic deformation is introduced in the liner when the cylinder is overstressed to the proof pressure level. In the unloading process (2→4), the cylinder pressure returns to 0. The composite wrap goes from A to C, where it remains in tension. It compresses the liner linearly from point 2 to point 3 and plastically to point 4. At this point, the balance between the composite wrap and the liner is established, and the compressive stress  $\sigma_c$  is introduced into the liner. During service ( $4 \leftrightarrow 4'$ ), the aluminum liner operates in ( $4 \leftrightarrow 4'$ ), and the composite wrap remains in (C↔B). The fracture analysis conducted here focuses on the service stage.

The selection of a proof pressure is crucial for the success of the autofrettage process. The following factors are considered in the process: (a) composite wrap strength, (b) liner material yielding strength, (c) Bauschinger effect, and (d) liner buckling. A maximum proof pressure selected should be smaller than the maximum pressure sustainable by the composite wrap, with a safety margin in case of damage to the composite. There is another trade-off for the selection of yielding strength of liner materials. The hysteresis loop is to be formed as the yielding strength is too low while not much compressive stress can be introduced if it is too high. In addition, the compressive yielding strength  $\sigma_c$  is affected by the Bauschinger effect which implies extremely high proof pressure may not

introduce high compressive stress in the liner. Furthermore, the compressive pressure introduced must not exceed the critical buckling stress of the liner wall, which can be expressed as [18]:

$$\sigma_{crit} = \frac{E}{\sqrt{3(1-\nu^2)}} \left( \frac{t}{R} \right) \quad (1)$$

where E is Young's modulus,  $\nu$  is Poisson's ratio, t is the wall thickness of the liner, and R is the cylinder radius.

## 2.2 Stress Intensity Factor (K) Evaluation

Since very few practical problems have closed-form stress intensity factor (K) solutions, numerical methods are widely used as an alternative for problems with complex geometric configurations and loadings. The approaches implemented in numerical evaluation generally fall into two categories: point matching and energy methods [19]. Point matching method derives from the formula of stress and displacement fields near the crack tip, but it requires a high degree of mesh refinement for reasonable accuracy. Earlier energy methods, such as J contour integration, elemental crack advance, and virtual crack extension, compute K based on the energy release rate in the body; however, separation of mixed-mode K components is difficult with these methods.

An interaction integral method is used in ABAQUS to extract the individual stress intensity factor (K) for a crack from the domain integral procedure [20-21]. This method is more accurate and efficient than earlier energy methods, and it is applicable to both isotropic and anisotropic linear materials under monotonic loading. The expression of K can be written as:

$$\vec{K} = 4\pi B \cdot \vec{J}_{\text{int}} \quad (2)$$

where  $\vec{K}$  is the K vector and  $\vec{J}_{\text{int}}$  is the interaction integral vector, both with three components according to three modes, and  $B$  is a pre-logarithmic energy factor matrix.

For homogeneous, isotropic materials,  $B$  is given by:

$$B = \begin{bmatrix} 8\pi(1-\nu^2)/E & 0 & 0 \\ 0 & 8\pi(1-\nu^2)/E & 0 \\ 0 & 0 & 4\pi/G \end{bmatrix} \quad (3)$$

where  $E$  is Young's modulus,  $\nu$  is Poisson's ratio, and  $G$  is the shear modulus.

The interaction integral vector  $\vec{J}_{\text{int}}$  is evaluated by the domain integral procedure and can be expressed as:

$$J_{\text{int}}^{\alpha} = \lim_{\Gamma \rightarrow \infty} \int_{\Gamma} \vec{n} \cdot M^{\alpha} \cdot \vec{q} d\Gamma \quad (4)$$

with  $M^{\alpha}$  given by:

$$M^{\alpha} = \sigma : \varepsilon_{aux}^{\alpha} I - \sigma \cdot \left( \frac{\partial \vec{u}}{\partial \vec{x}} \right)_{aux}^{\alpha} - \sigma_{aux}^{\alpha} \cdot \frac{\partial \vec{u}}{\partial \vec{x}} \quad (5)$$

where  $\alpha$  is equal to I, II, and III according to the three modes of fracture mechanics,  $\Gamma$  is the contour that encloses the crack tip,  $\vec{n}$  is the outward normal of  $\Gamma$ ,  $\vec{q}$  is the crack extension direction,  $\vec{u}$  is the displacement vector,  $\vec{x}$  is the coordinate vector,  $I$  is the identity matrix, and  $\sigma$ ,  $\sigma_{aux}^{\alpha}$  and  $\varepsilon_{aux}^{\alpha}$  are stress, auxiliary stress, and strain respectively.

### 2.3 J-Integral Evaluation

The energy domain integral method is formulated in [22] to provide a general framework for numerical analysis of the J-integral. This method has been adopted by ABAQUS for its easier numerical implementation and higher accuracy with coarser mesh compared with earlier energy methods. In the domain integral technique, a closed contour

$(C + C_+ + \Gamma + C_-)$  is constructed around the crack as illustrated in Figure 3. The inner contour  $\Gamma$  is vanishingly small, while the outer contour  $C$  is finite. Using the divergence theorem, the 2D quasi-static contour integral is converted to domain integral on closed area  $A$ , which is defined by:

$$J = -\int_A \frac{\partial}{\partial \vec{x}} \cdot (H \cdot \bar{q}) d\Gamma - \int_{C_+ + C_-} \vec{t} \cdot \frac{\partial \vec{u}}{\partial \vec{x}} \cdot \bar{q} d\Gamma \quad (6)$$

with tensor  $H$  given by:

$$H = WI - \sigma \cdot \frac{\partial \vec{u}}{\partial \vec{x}} \quad (7)$$

where  $\vec{t}$  is the surface traction force,  $\bar{q}$  is equal to  $\bar{q}$  on  $\Gamma$  and vanishes on  $C$ , and  $W$  is the strain energy. For elasto-plastic material, plastic dissipation is also included in  $W$ , which implies that the J-integral calculation of this condition is applicable only for monotonic loading. The 3D domain integral can be obtained by expanding a 2D contour along crack front  $S$  for a virtual distance  $dS$  to form an integral on volume  $V$ .

The ABAQUS software defines the domain in terms of rings of elements surrounding the crack tip [21]. The first contour consists of those elements directly connected to crack-tip nodes. The second contour includes the elements in the first contour and the next ring of elements that share nodes with the elements in the first contour. Each subsequent contour is defined by adding the next ring of elements that share nodes with the elements in the previous contour.

## 2.4 Material Models

Several material models are used in the simulation to describe the behavior of the cylinder wall. The composite wrap is formulated by doubly curved laminated shell theory with an orthotropic material constitutive model given by:

$$\begin{Bmatrix} \varepsilon_{11} \\ \varepsilon_{22} \\ \varepsilon_{33} \\ \varepsilon_{12} \\ \varepsilon_{13} \\ \varepsilon_{23} \end{Bmatrix} = \begin{bmatrix} 1/E_1 & -\nu_{12}/E_1 & -\nu_{13}/E_1 & 0 & 0 & 0 \\ -\nu_{12}/E_1 & 1/E_2 & -\nu_{23}/E_2 & 0 & 0 & 0 \\ -\nu_{13}/E_1 & -\nu_{23}/E_2 & 1/E_3 & 0 & 0 & 0 \\ 0 & 0 & 0 & 1/G_{12} & 0 & 0 \\ 0 & 0 & 0 & 0 & 1/G_{13} & 0 \\ 0 & 0 & 0 & 0 & 0 & 1/G_{23} \end{bmatrix} \begin{Bmatrix} \sigma_{11} \\ \sigma_{22} \\ \sigma_{33} \\ \sigma_{12} \\ \sigma_{13} \\ \sigma_{23} \end{Bmatrix} \quad (8)$$

where  $E_i$  is Young's moduli,  $G_{ij}$  is the shear moduli, and  $\nu_{ij}$  is Poisson's ratios.

To simulate the autofrettage process, an elasto-plastic material model is used to capture deformation of the aluminum liner in the global model. The nonlinear isotropic/kinematic hardening law is employed to account for the Bauschinger effect. The yield surface is governed by the Mises flow rule:

$$f(\sigma - \alpha) - \sigma_y = 0 \quad (9)$$

with equivalent Mises stress given by:

$$f(\sigma - \alpha) = \sqrt{\frac{3}{2} (S - \alpha^{dev}) : (S - \alpha^{dev})} \quad (10)$$

where  $\alpha$  is the back stress,  $\alpha^{dev}$  is the back stress deviator, and  $S$  is the stress deviator.

The hardening law is given by:

$$\dot{\alpha} = C \frac{1}{\sigma_y} (\sigma - \alpha) \dot{\varepsilon}^{pl} - \gamma \alpha \dot{\varepsilon}^{pl} \quad (11)$$

where  $\dot{\alpha}$  is the back stress rate,  $\dot{\varepsilon}^{pl}$  is the equivalent plastic strain rate,  $C$  is the kinematic modulus, and  $\gamma$  is the slip rate.  $C$  and  $\gamma$  are calibrated by material test data.

In the submodel, different elastic models are implemented for the aluminum liner according to computational requirement of fracture parameters. To extract  $K$  along the crack front, linear elastic material model is required by the interaction integral method. Instead of using an elasto-plastic model, Ramberg-Osgood (R-O) nonlinear elastic model is used in J-integral evaluation, thus eliminating the loading effect on the accuracy of

domain integration. The one-dimension expression of the R-O model can be expressed as:

$$\frac{\varepsilon}{\varepsilon_0} = \frac{\sigma}{\sigma_0} + \alpha \left( \frac{\sigma}{\sigma_0} \right)^n \quad (12)$$

where  $\alpha$  is a dimensionless constant and  $n$  is the strain hardening exponent. The model is directly related to the description of the singularity field around the crack tip and it is widely used for curve-fitting the stress-strain data. The 3D format, used in the simulation, can be expanded from Eq.(12) as:

$$E\varepsilon = (1+\nu)S - (1-2\nu)pI + \frac{3}{2}\alpha \left( \frac{q}{\sigma_0} \right)^{n-1} S \quad (13)$$

where  $E$  is Young's modulus,  $\nu$  is Poisson's ratio,  $p$  is the equivalent hydrostatic stress,  $q$  is the von-Mises equivalent stress, and  $S$  is the stress deviator.

Distinction between the K dominance and J-integral dominance is characterized by the size of the plastic zone in the vicinity of the crack tip. The radius of a critical plastic zone is given by:

$$r_p = \frac{1}{6} \left( \frac{K_{IC}}{\sigma_y} \right)^2 \quad (14)$$

where  $K_{IC}$  is the mode I fracture toughness and  $\sigma_y$  is the yielding strength. The domain of the plastic zone is obtained by identifying the region where the asymptotic stress ahead of the crack tip equals the yielding stress.

### 3. FINITE ELEMENT SIMULATION

The semi-elliptical crack is required to be modeled in substantial detail to obtain precise values of fracture parameters. If the crack were modeled together with the whole cylinder, the resulting element size would be too small and the model would be too large. Along with the complexity of wall structure and material nonlinearity, it would demand tremendous computational cost. This restriction is resolved by a global-local FE analysis strategy. The global model with coarse mesh is used to obtain the displacement solution of the liner crack region. The local model of the region surrounding the crack is created with a very fine mesh. The boundary conditions of the local model are driven by the solution of global analysis.

The dimensions considered in the present analysis are based on a design typical of those described in literature [2]. The outer radius of the cylinder  $R_{out}$  is 0.229 m and the inner radius  $R_{in}$  is 0.217 m (Figure 1). The carbon/epoxy wrap consists of helical and hoop laminates resulting in a total composite shell thickness ( $t_c$ ) of 9 mm, and the thickness of the liner ( $t_a$ ) is 2.54 mm. The material properties are summarized in Tables 1 and 2 [2, 23]. Study cases with various flaw sizes and proof pressures are summarized in Table 3.

#### 3.1 Global Model

For symmetry, one eighth of the cylinder is modeled, and symmetric boundary conditions are imposed on the cut sides. The laminated composite wrap is modeled using a doubly curved 8-node shell element and the liner by an 8-node solid brick element. Reduced integration is used to improve both computational efficiency and bending analysis accuracy. Figure 4 shows a schematic of the mesh for the whole cylinder model.

A finer mesh is used in the region, to which the local model will be applied. The wall is constructed by tying the shell element to the brick element surface with an offset of a half shell thickness. The lay-up of composite wrap ( $[\pm 10^\circ / 90^\circ]_3$ ) consists of six helical plies alternated with three hoop plies (in Figure 4). The thickness of each helical ply is 0.55 mm and each hoop ply is 1.9 mm in order to match the design stress ratio 0.8 (stress in the helical layer/stress in the hoop layer). The material direction of the aluminum liner is 1 in the hoop and 2 in the axial direction. Pressure loading is applied on the entire inner surface of the liner.

### 3.2 Local Model

To evaluate the fracture parameters for the axial crack, a local FE model is created for a small portion of the liner wall containing a crack (Figure 5). The size of the region is approximately that of one element in the global model (marked in Figure 4). The geometry of the region is the same as the corresponding portion in the global model. In consideration of the crack symmetry, only half the crack is modeled. Quadratic continuum elements with 20 nodes (C3D20R in ABAQUS) are employed for better accuracy and better representation of the crack front curvature. The mesh density is significantly higher than that for the global model, and the crack tip is surrounded by many layers of elements. Singular continuum elements with a collapsed face are used to model the crack tip. For computation of  $K$ ,  $1/\sqrt{r}$  singularity is created using quarter-point nodes, where  $r$  is the distance to the crack tip. When the J-integral is evaluated, the nodes at crack tip are duplicated to create the combined  $1/\sqrt{r}$  and  $1/r$  singularity for power-law hardening.



Figure 5 shows the local FE model of the region containing a crack. The bottom face and the area below the crack front on the front face are applied with pressure loading. Boundary conditions of the top, back, and right faces are determined by displacement results of the global analysis. Symmetric constraints are imposed on the left face and the area above the crack front on the front face. The transfer of global analysis results to local analysis is achieved using the sub-modeling procedure of ABAQUS software.

### **3.3 Simulation Procedure**

The implementation scheme of the simulation procedure is illustrated in Figure 6. The entire simulation is performed in three steps. The data swap between steps is assisted by ABAQUS subroutines and the submodel technique. The procedure is executed automatically by the control of Matlab software.

Step 1: The autofrettage process is simulated in the global model by applying cyclic pressure loading. A stress state (marked as ‘ $\otimes$ ’ in Figure 2) is selected and will be exported to the second step analysis as initial stress. Since the domain integral method in ABAQUS does not consider the initial stress, the stress in the liner is chosen to be close to zero in the selected stress state. The stress state selected for the model is recorded to a file using the ABAQUS user subroutine UVARM.

Step 2: The displacement field needed for the submodel is computed from the global model with a monotonic pressure loading applied from zero to operating pressures. The autofrettage effect is introduced by applying the initial stresses in the model. From the file created in Step 1, the initial stresses are read in using the ABAQUS user subroutine SIGINI.

Step 3: The fracture parameters are extracted from the local model. The model is driven by the boundary displacement computed from Step 2. Monotonic pressure loading identical to that in Step 2, is applied on the crack open face. Various material models are implemented with a linear elastic model for K computation and an R-O model for J-integral evaluation.

## **4. RESULTS AND DISCUSSION**

### **4.1 Autofrettage Process Simulation**

The far-field von-Mises stress distribution of the liner with four autofrettage levels is shown in Figure 7. The stresses are plotted as a function of pressure loading increment. The pressure load increases linearly to proof pressure in the first ten increments (Interval 1), decreases to 0 in the next 10 increments (Interval 2), and rises back to operating pressure in the last 10 increments (Interval 3). The yielding occurs during Interval 1, and a higher stress level is obtained by a higher proof pressure due to material hardening. When pressure returns to 0 at 20<sup>th</sup> increment, residual stresses are introduced by compression of the composite wrap. Higher residual stresses occur at higher proof pressure. At the 30<sup>th</sup> increment, when it rises back to operating pressure, lower stresses remain in higher proof pressure cases.

Figure 8 illustrates cyclic far-field stress-strain curves for the liner at four autofrettage levels according to the loading sequence described in Figure 7. The stress/strain aligns in the hoop direction which is perpendicular to the crack face. The deformation routes of four autofrettage levels are listed in the lower right corner of the figure. It can be seen that higher compressive stress is introduced when higher proof pressure is applied, and

the opposite is taken for the tensile stresses. The variation of the introduced compressive stresses is proportional to proof pressure with the exception to the case of  $P_f = 2.0 \cdot P_o$ . The reason is that the first three cases do not reach the compressive yielding strength and return linearly, and the last case yields at point 5'. Also, the Bauschinger effect can be observed at point 5', where the yielding stress is less than that at point 1. Furthermore, the four cases satisfy all constraints specified in section 2.1 and the selected stress fields are exported for the subsequent step analysis.

#### 4.2 Stress Intensity Factor (K) and J-integral

In the present section, results along the crack front are normalized to  $\theta$  as shown in the inset in Figure 9. Stress intensity factor (K) and the J-integral along the crack front are reported in Figures 9 and 10 respectively with four selected autofrettage levels. The values of both K and the J-integral at a higher  $\theta$  are much larger than those at a lower  $\theta$ . This implies that the crack grows faster in the center so that the elliptic shape tends to be stretched closer to a circular shape. It can also be observed that the autofrettage process dramatically reduces the values of both K and the J-integral.

Figures 11 and 12 plot K and the J-integral against the internal pressure loading. The dotted horizontal lines mark the critical values of parameters (or fracture toughness)  $K_c$  and  $J_c$ . At the beginning, values of fracture parameters are equal to zero, indicating the crack is compressed to closure status by the composite wrap. With the internal pressure increasing enough to overcome the compressive stress, the crack changes to the opening status. Value of stress intensity factor increases with loading linearly, while that of J-integral increases nonlinearly. Furthermore, the crack for case  $P_f = 1.0 \cdot P_o$  may stay in unstable growth condition since both the J-integral and K are above critical values.

Figures 13 to 16 show  $K$  and the J-integral along the crack front with various geometric ratios when the proof pressure is equal to 1.5 times the operating pressure. Figures 13 and 14 show the results of cracks with same shape (depth/width ratio) but different sizes (depth/thickness ratio). It can be seen that the crack size significantly affects fracture performance and fracture parameters of a larger crack have much higher values. Figures 15 and 16 show the results of cracks with the same size and different shapes. When the crack shape becomes closer to a circle (higher depth/width ratio), the curve of fracture parameters becomes flatter. Crack growth speed along crack front is almost same when  $a/c$  is equal to 0.75. However, when  $a/c$  is equal to 0.25, the center part of the crack grows much faster than two sides.

#### 4.3 Stress Field Characterization on the Crack Tip Vicinity

Figure 17 shows the stress distribution around the crack tip of a typical loading condition. The stress is relaxed in the area under the crack tip near the free crack surface, while it is concentrated in the front of crack tip with an oblique angle where the plastic zone is formed. In Figure 18, three locations along the crack front curve, identified as A, B, and C, are selected to illustrate plastic zone shape and stress distribution. A plane strain like plastic zone is developed at A, takes transition around the B and turns into the shape of a typical plain stress plastic zone at C.

Figure 19 shows the size of the plastic zone with four autofrettage levels at A and C. The critical plastic zone size is characterized by the radius  $r_{pc}$  computed from Eq.(14) and marked by dotted circles. It can be seen that large scale yielding occurs when  $P_f=1.0 \cdot P_0$ . The plastic zone grows out of the  $2 r_{pc}$  region, indicating fracture failure may occur by unstable crack growth. When  $P_f=1.25 \cdot P_0$ , the size of the plastic zone is large, compared

with dimensions of the crack length and the remaining ligament, which implies a contained yielding condition. When  $P_f = 1.5 \cdot P_0$ , the plastic zone size is small enough for the J-dominated stress field to be developed around the crack tip and the crack tip condition can be characterized by the J-integral. Based on the ASTM standard, the case of  $P_f = 2.0 \cdot P_0$  can be safely characterized by one K parameter since the size of its plastic zone is at least fifteen times smaller than the other dimensions.

## 5. CONCLUSIONS

A comprehensive finite element model has been developed to predict the fracture behavior of high pressure composite cylinders for hydrogen storage. The simulation of the autofrettage process is carried out in the global model. Plastic hardening and Bauschinger effect are observed in the results. Both stress intensity factor (K) and the J-integral are computed along the crack front in the local model with consideration of autofrettage influence and crack size effect. Results show that the autofrettage process significantly improves the cylinder fracture performance, and the smaller crack size reduces the values of the fracture parameters dramatically. Shape and size of the plastic zone around the crack tip are examined. Fracture behavior is evaluated by observation of the plastic zone, and the corresponding parameter characterization is analyzed. The developed model and the proposed methodology can be used for design guidance to improve cylinder fracture performance with consideration of autofrettage process, and developing a fracture parameter database for fatigue life prediction.

**REFERENCES**

- [1] D. Chapelle and D. Perreux, "Optimal Design of a Type 3 Hydrogen Vessel: Part I- Analytic Modeling of the Cylindrical Section," *International Journal of Hydrogen Energy*, Vol.31, pp. 627–638, 2006.
- [2] F. Mitlitsky, A. H. Weisberg and B. Myers, "Vehicular Hydrogen Storage using Lightweight Tanks, " *Proceedings of the 2000 U.S.DOE Hydrogen Program Review*, NREL/CP-570-28890, 2000.
- [3] H. Kobayashi, S. Sakai, M. Asano, K. Miyazaki, T. Nagasaki and Y. Takahashi, "Development of a Flaw Evaluation Handbook of the High Pressure Institute of Japan," *International Journal of Pressure Vessels and Piping*, Vol.77, pp.929-936, 2000.
- [4] A. R. Shahani and S. E. Habibi, "Stress Intensity Factors in a Hollow Cylinder Containing a Circumferential Semi-elliptical Crack Subjected to Combined Loading," *International Journal of Fatigue*, Vol. 29, pp.128-140, 2007.
- [5] J. H. Underwood, "Stress Intensity Factor for Internally Pressurized Thick Walled Cylinders," *ASTM STP*, Vol. 513, pp. 59–70, 1972.
- [6] I. S. Raju and J. C. Newman, "An Empirical Stress Intensity Factor Equation for the Surface Crack," *Engineering Fracture Mechanics*, Vol.15, pp. 185-192, 1981.
- [7] T. Fett, "Estimation of Stress Intensity Factors for Semi-elliptical Surface Cracks," *Engineering Fracture Mechanics*, Vol. 66, pp.349-356, 2000.
- [8] J. R. Rice and N. Levy, "The Part-through Surface Crack in an Elastic Plate," *Journal of Applied Mechanics*, ASME, Vol. 39, pp.185-194, 1972.
- [9] H. Lee and M. Parks, "Enhanced Elastic-plastic Line-spring Finite Element," *International Journal of Solids and Structures*, Vol. 32, pp. 2393-2418, 1995.
- [10] I. S. Raju and J. C. Newman, "Stress-intensity Factor for Internal and External Surface Cracks in Cylindrical Vessels," *International Journal of Pressure Vessel Technology*, Vol.104, pp.293-298, 1982.

- [11] Y-J Kim, J-S Kim, Y-J Park and Y-J Kim, “Elastic–plastic Fracture Mechanics Method for Finite Internal Axial Surface Cracks in Cylinders,” *Engineering Fracture Mechanics*, Vol.71, pp.925-944, 2004.
- [12] A. Th. Diamantoudis and G. N. Labeas, “Stress Intensity Factors of Semi-elliptical Surface Cracks in Pressure Vessels by Global-local Finite Element Methodology,” *Engineering Fracture Mechanics*, Vol. 72, pp.1299-1312, 2005.
- [13] M. A. Guerrero, C. Betegon and J. Belzunce, “Fracture Analysis of a Pressure Vessel Made of High Strength Steel (HSS),” *Engineering Failure Analysis*, Vol.15, pp.208-219, 2008.
- [14] B. Su and G. S. Bhuyan, “The Fracture Behavior of the Aluminum Lined Hoop-wrapped Cylinders with Internal Axial Cracks,” *International Journal of Pressure Vessels and Piping*, Vol. 76, pp.251-257, 1999.
- [15] B. Su, Ch. Li and G. S. Bhuyan, “Comparison between Fractures Parameters of an All-aluminum Cylinder with Cracks under Different Deformation Conditions,” *International Journal of Pressure Vessels and Piping*, Vol.77, pp. 179-184, 2000.
- [16] A. R. Shahani and M. M. Kheirikhah, “Stress Intensity Factor Calculation of Steel-lined Hoop-wrapped Cylinders with Internal Semi-elliptical Circumferential Crack,” *Engineering Fracture Mechanics*, Vol.74, pp. 2004-2013, 2007.
- [17] M. Z. Kabir, “Finite Element Analysis of Composite Pressure Vessels with a Load Sharing Metallic Liner,” *Composite Structures*, Vol. 49, pp. 247-255, 2000.
- [18] G. W. Hunt, G. J. Lord and M. A. Peletier, “Cylindrical Shell Buckling: A Characterization of Localization and Periodicity,” *Discrete and Continuous Dynamical Systems – Series B*, Vol. 3, pp. 505-518, 2003.
- [19] T. L. Anderson, *Fracture mechanics: Fundamentals and Applications*. Boca Raton, Florida: CRC Press, 1995.
- [20] C. F. Shih and R. J. Asaro, “Elasto-plastic Analysis of Cracks on Bi-material Interfaces: Part I–Small Scale Yielding,” *Journal of Applied Mechanics*, ASME, Vol. 55, pp. 299–316, 1988.
- [21] ABAQUS version 6.7. Pawtucket, RI: Hibbitt, Karlsson & Sorensen Inc, 2007.

- [22] B. Moran and C. F. Shih, "A General Treatment of Crack Tip, Contour Integrals," *International Journal of Fracture*, Vol. 35, pp.295–310, 1987.
- [23] J. B. Jordon, M. F. Horstemeyer, K. Solanki and Y. Xue, "Damage and Stress State Influence on the Bauschinger Effect in Aluminum Alloys," *Mechanics of Materials* Vol. 39, pp. 920–931 2007.



**LIST OF TABLES**

Table 1 Mechanical properties of carbon/epoxy composite

Table 2 Mechanical properties of Aluminum Alloy 7075-T651

Table 3 Summary of study cases

**LIST OF FIGURES**

- Figure 1 Schematic of hydrogen composite cylinder
- Figure 2 Diagram of autofrettage process
- Figure 3 Schematic of domain integral evaluation
- Figure 4 Global finite element model
- Figure 5 Local finite element model
- Figure 6 Implementation scheme
- Figure 7 von-Mises stress distribution in liner
- Figure 8 Cyclic stress-strain curves for various autofrettage levels
- Figure 9 Stress intensity factor (K) along crack front for various autofrettage levels
- Figure 10 J-integral along crack front for various autofrettage levels
- Figure 11 Stress intensity factor (K) against pressure loading for various autofrettage levels
- Figure 12 J-integral against pressure loading for various autofrettage levels
- Figure 13 Stress intensity factor (K) along crack front with various geometric ratios
- Figure 14 J-integral along crack front with various geometric ratios
- Figure 15 Stress distribution of the crack front vicinity
- Figure 16 Transition of plastic zone shapes along crack front
- Figure 17 Plastic zone shapes for various autofrettage levels

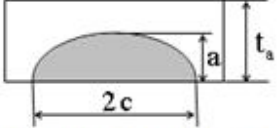
Table 1 Mechanical properties of carbon/epoxy composite

Properties	Values
$E_1$ (GPa)	156.5
$E_2, E_3$ (GPa)	7.23
$G_{12}, G_{13}$ (GPa)	4.12
$G_{23}$ (GPa)	3.35
$\nu_{12}, \nu_{13}$	0.337
$\nu_{23}$	0.4
Fiber strength (MPa)	5100

Table 2 Mechanical properties of Aluminum Alloy 7075-T651

Properties	Values
E (GPa)	71.7
$\nu_{12}$	0.33
$\sigma_y$ (MPa)	520
$\sigma_c$ (MPa)	430
$n$	25
$\alpha$	0.3
C (GPa)	7.0
$\gamma$	40

Table 3 Summary of study cases

Case No.	Depth/thickness ( $a/t_a$ )	Depth/width ( $a/c$ )	Proof pressure, $P_f$	Description
1	0.50	0.25	1.00 $P_o$	 <p>Operating pressure, <math>P_o</math> is 34.5 MPa</p>
2			1.25 $P_o$	
3			1.50 $P_o$	
4			2.00 $P_o$	
5	0.25	0.25	1.50 $P_o$	
6	0.75			
7	0.50	0.50		
8	0.50	0.75		

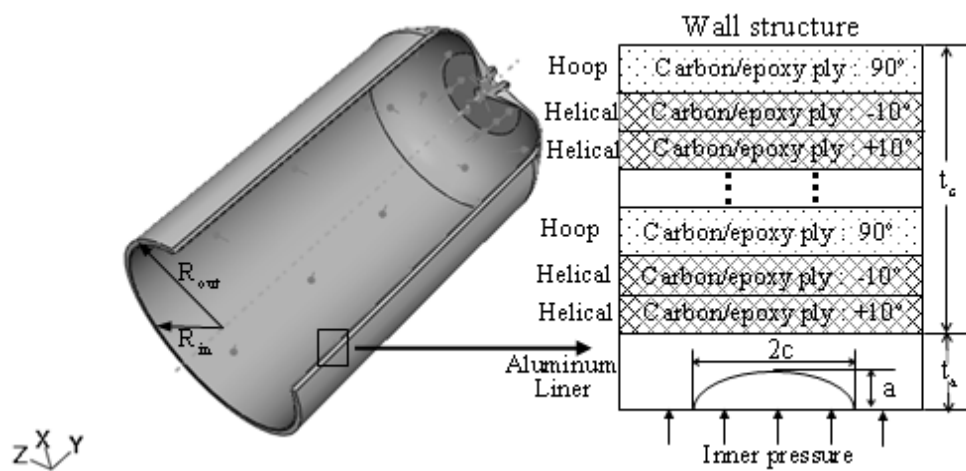


Figure 1 Schematic of hydrogen composite cylinder

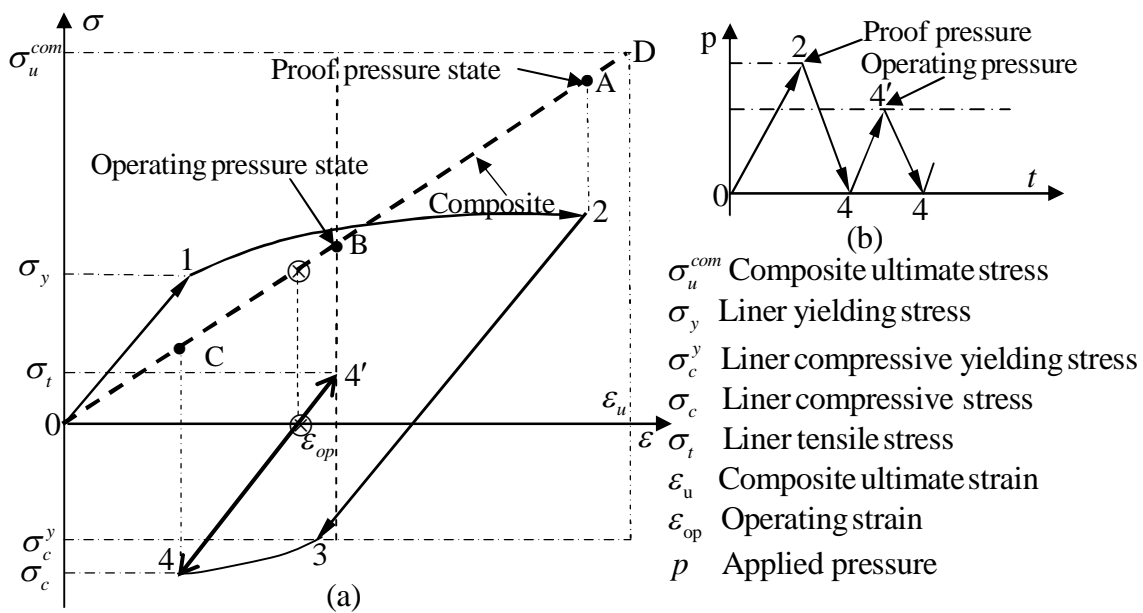


Figure 2 Diagram of autofrettage process

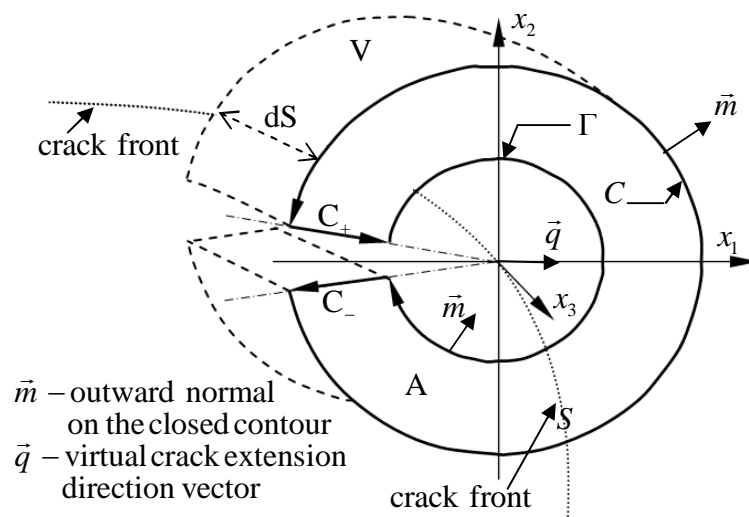


Figure 3 Schematic of domain integral evaluation



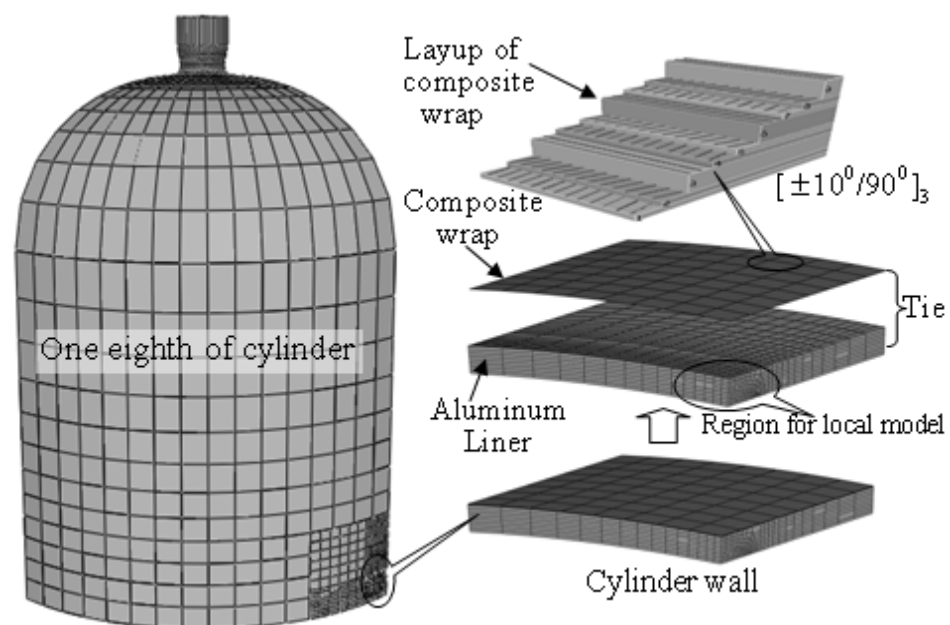


Figure 4 Global finite element model

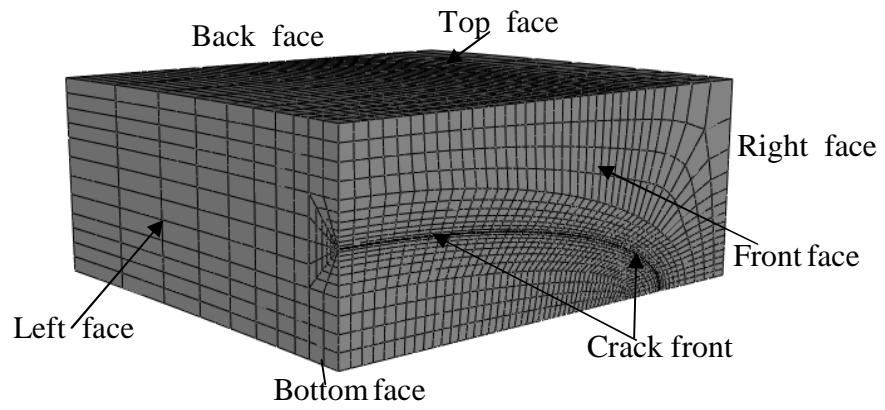


Figure 5 Local finite element model

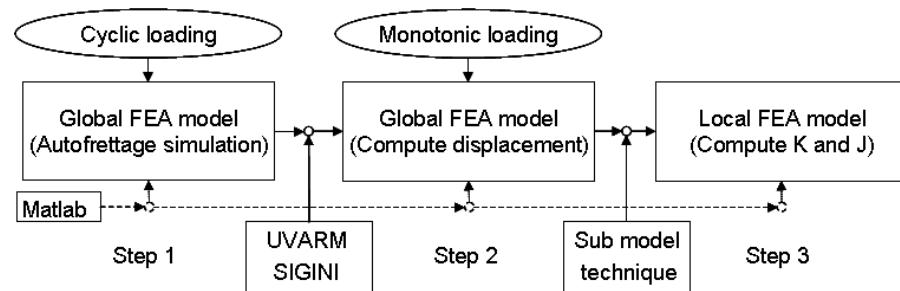


Figure 6 Implementation scheme

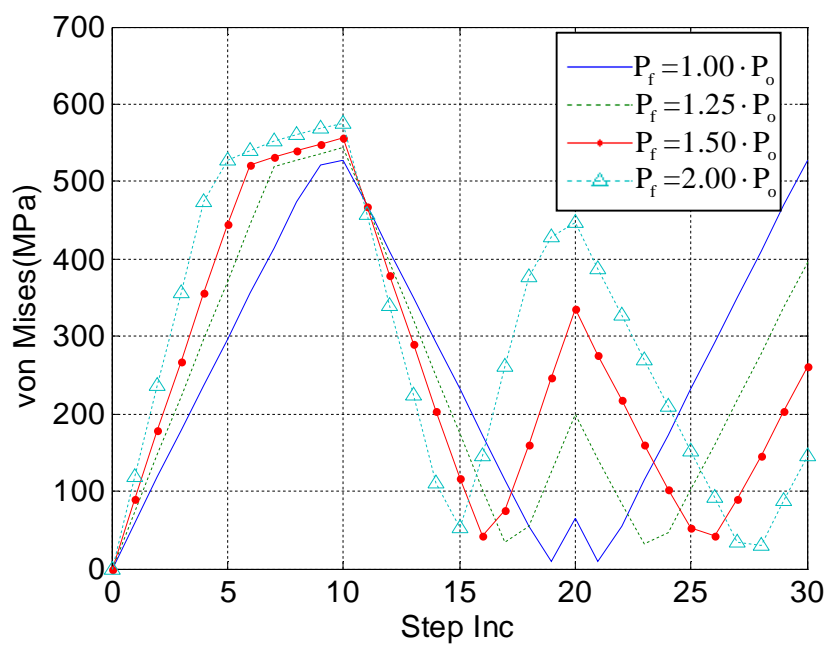


Figure 7 von-Mises stress distribution in liner

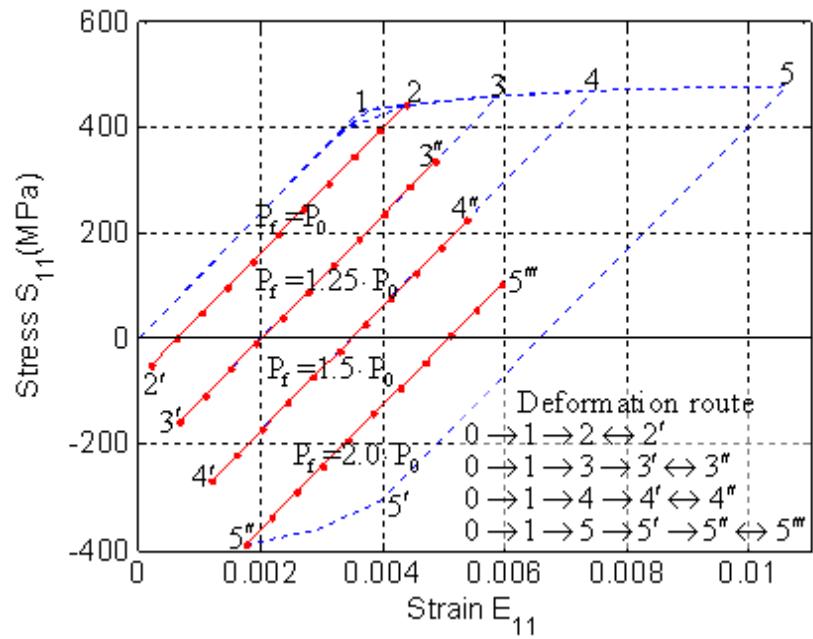


Figure 8 Cyclic stress-strain curves for various autofrettage levels

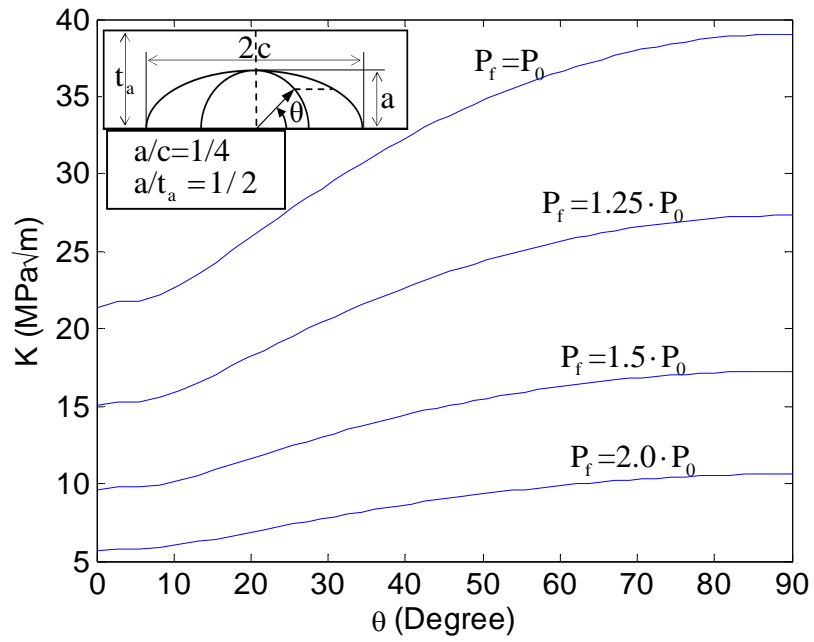


Figure 9 Stress intensity factor (K) along crack front for various autofrettage levels

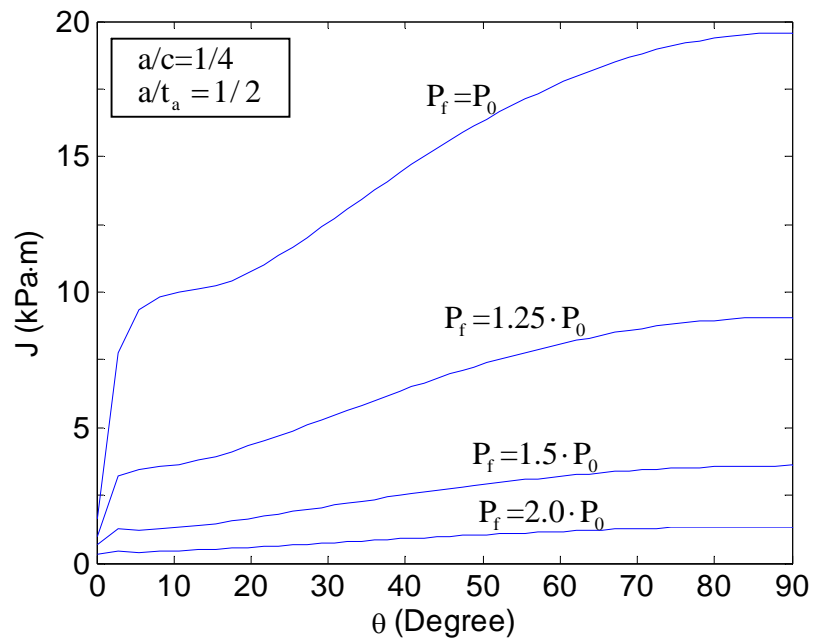


Figure 10 J-integral along crack front for various autofrettage levels

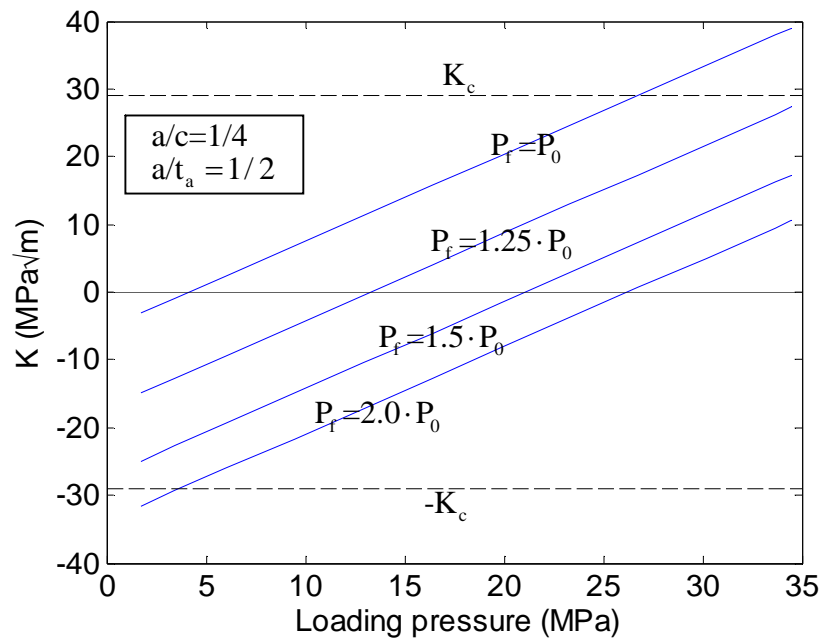


Figure 11 Stress intensity factor ( $K$ ) against pressure loading for various autofrettage levels



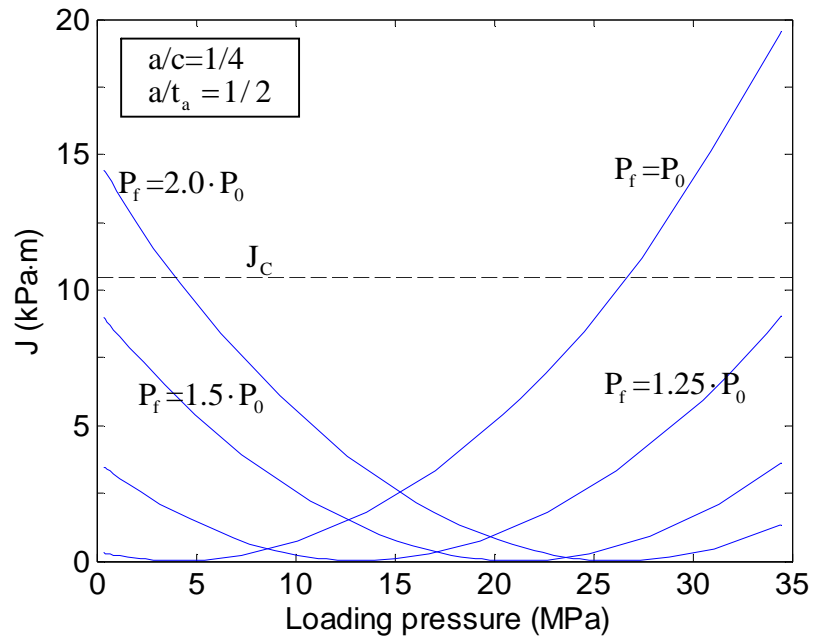


Figure 12 J-integral against pressure loading for various autofrettage levels

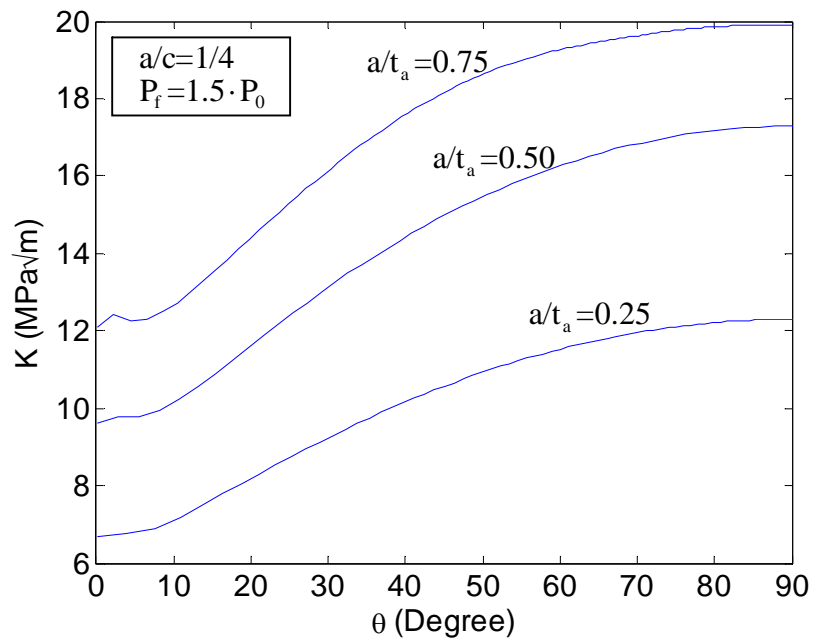


Figure 13 Stress intensity factor (K) along crack front with various geometric ratios

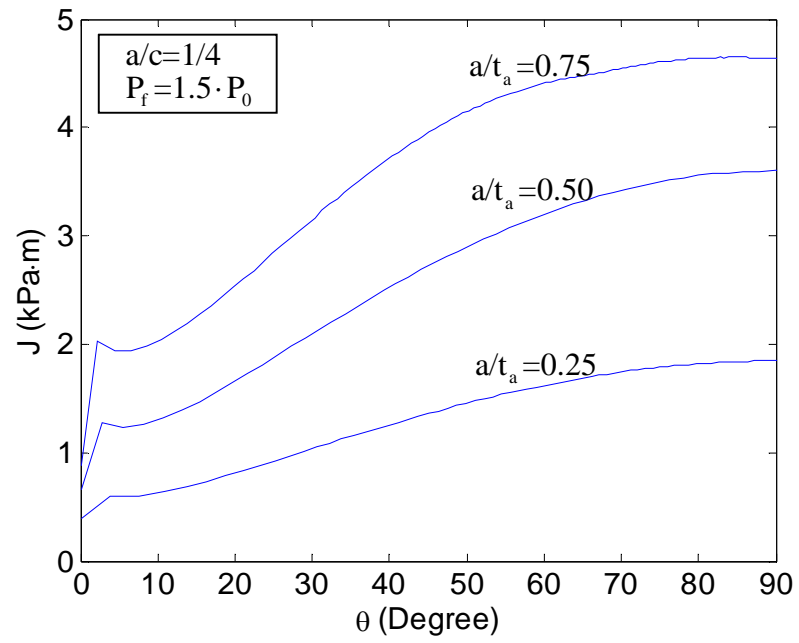


Figure 14 J-integral along crack front with various geometric ratios

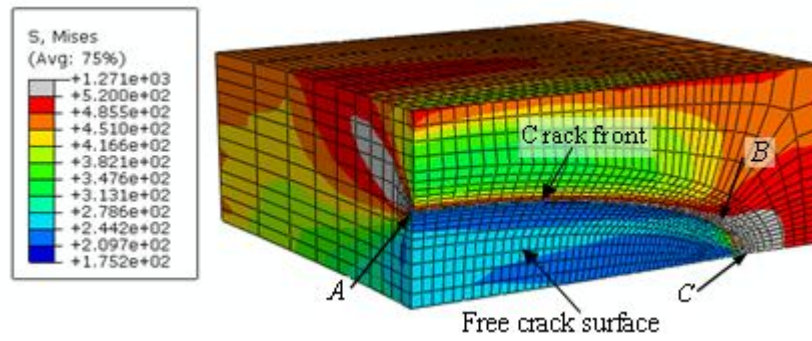


Figure 15 Stress distribution of the crack front vicinity

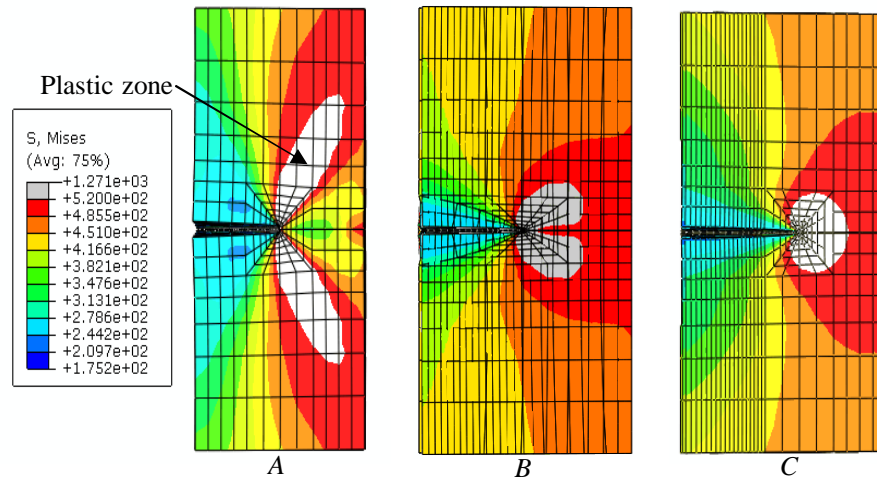


Figure 16 Transition of plastic zone shapes along crack front

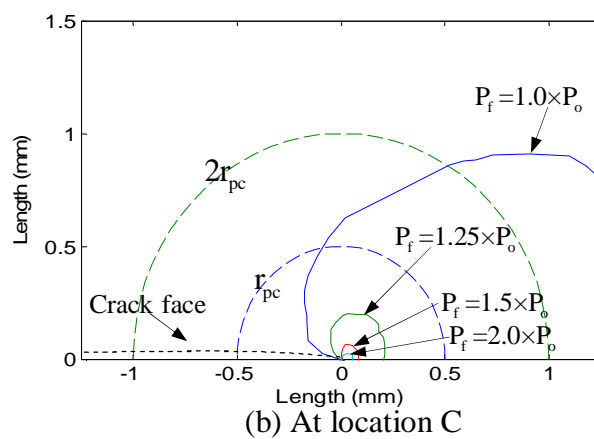
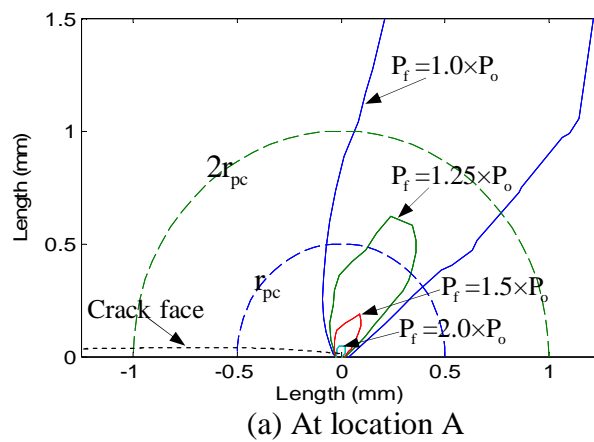


Figure 17 Plastic zone shapes for various autofrettage levels

**BIBLIOGRAPHY**

- [1] Züttel, "Materials for Hydrogen Storage," *Materials Today*, Vol.6, pp.24-33, 2003.
- [2] N. Takeichi, H. Senoh and T. Yokota, "'Hybrid Hydrogen Storage Vessel', a Novel High-pressure Hydrogen Storage Vessel Combined with Hydrogen Storage Material," *International Journal of Hydrogen Energy*, Vol.28, pp.1121-1129, 2003.
- [3] E. David, "An Overview of Advanced Materials for Hydrogen Storage," *Journal of Materials Processing Technology*, Vol.162-163, pp.169-177, 2005.
- [4] J. M. Lifshitz and H. Dayan, "Filament-wound Pressure Vessel with Thick Metal Liner," *Composite Structures*, Vol.32, pp.313-323, 1995.
- [5] D. V. Rosato and C. S. Grove "Filament Winding, Its Development, Manufacture, Applications and Design," New York: Interscience, 1964.
- [6] A. M. Shibley, "Filament winding, Handbook of Fiber-glass and Advanced Plastic Materials," New York: Van Nostrand Reinhold, 1969.
- [7] S. T. Peters, W. D. Humphrey and R. F. Foral, "Filament Winding Composite Structure Fabrication," *Advancement of Material and Process Engineering*, SAMPE International Business Office, 1991.
- [8] S. G. Lekhnitskii, "Theory of Elasticity of an Anisotropic Body," Moscow: Mir Publishers, 1981.
- [9] J. Mistry, A. G. Gibson and Y-S. Wu, "Failure of Composite Cylinders under Combined External Pressure and Axial Loading," *Composite Structures*, Vol.22, pp.193-200, 1992.
- [10] P. D. Soden, R. Kitching, P. C. Tse, M. J. Hinton and Y. Tsavalas, "Influence of Winding Angle on the Strength and Deformation of Filament-wound Composite Tubes Subjected to Uniaxial and Biaxial Loads," *Composites Science and Technology*, Vol.46, pp.363-378, 1993.
- [11] M. F. S. Al-Khalil, P. D. Soden, R. Kitching and M. J. Hinton, "The Effects of Radial Stresses on the Strength of Thin-walled Filament Wound GRP Composite Pressure Cylinders," *International Journal of Mechanical Science*, Vol.38, pp.97-120, 1996.
- [12] P. M. Wild and G. W. Vickers, "Analysis of Filament-wound Cylindrical Sheels under Combined Centrifugal, Pressure and Axial Loading," *Composite Part A*, Vol.28, pp.47-55, 1997.

- [13] L. Parnas and N. Katić, "Design of Fiber-reinforced Composite Pressure Vessels under Various Loading Conditions," *Composite Structure*, Vol.58, pp.83-95, 2002.
- [14] H. Akcay and I. Kaynak, "Analysis of Multilayered Composite Cylinders under Thermal Loading," *Journal of Reinforced Plastics and Composites*, Vol. 24, pp.1169-1179, 2005.
- [15] O. Sayman, "Analysis of Multi-layered Composite Cylinders under Hydrothermal Loading," *Composites: Part A*, Vol.36, pp.923-933, 2005.
- [16] P. Y. Tabakov, "Design of Laminated Cylinders using Genetic Algorithm," *Journal of Applied Computer Science*, Vol.8, pp.7-29, 2000.
- [17] P. Y. Tabakov and E. B. Summers, "Lay-up Optimization of Multilayered Anisotropic Cylinders based on a 3-D Elasticity Solution," *Computers and Structures*, Vol.84, pp.374-384, 2006.
- [18] D. Chapelle and D. Perreux, "Optimal Design of a Type 3 Hydrogen Vessel: Part I- Analytic Modeling of the Cylindrical Section," *International Journal of Hydrogen Energy*, Vol.31, pp.627- 638, 2006.
- [19] S. V. Hoa, C. H. Yu and T. S. Sankar, "Analysis of Filament Wound Vessel Using Finite Elements," *Composite Structures*, Vol. 3, pp.1-18, 1985.
- [20] J. Park, C. Hong, C-G. Kim and C-U. Kim, "Analysis of Filament Wound Composite Structures considering the Change of Winding Angles through the Thickness Direction," *Composite Structures*, Vol. 55, pp.63-71, 2002.
- [21] M. Z. Kabir, "Finite Element Analysis of Composite Pressure Vessels with a Load Sharing Metallic Liner," *Composite Structures*, Vol. 49, pp. 247-255, 2000.
- [22] H. T. Walter, P. S. Griffin and A. C. Jackson, "Design and Manufacture of a Composite Overwrapped Pressurant Tank Assembly," 38th AIAA/ASME/SAE/ASEE Joint Propulsion Conference & Exhibit, Indianapolis, Indiana, AIAA 2002-4349, pp.1-12, 2002.
- [23] D. L. Gray and D. J. Moser, "Finite Element Analysis of a Composite Overwrapped Pressure Vessel," 40th AIAA/ASME/SAE/ASEE Joint Propulsion Conference and Exhibit, Fort Lauderdale, Florida, AIAA 2004-3506, pp.1-15, 2004.
- [24] U. Kim, J. Kang, C. Hong and C. G. Kim, "Optimal Design of Filament Wound Structures under Internal Pressure based on the Semi-geodesic Path Algorithm," *Composite Structures*, Vol. 67, pp.443-452, 2005.



- [25] Y. D. Doh and C. S. Hong, "Progressive Failure Analysis for Filament Wound Pressure Vessel," *Journal of Reinforced Plastics and Composites*, Vol.14, pp.1278-1306, 1995.
- [26] C. Chamis, P. K. Gotsis and L. Minnetyan, "Progressive Fracture and Damage Tolerance of Composite Pressure Vessels," *Proceedings of The International Composites Expo*, Session 5-C, pp.1-8, 1997.
- [27] L. Minnetyan, P. K. Gotsis and C. C. Chamis, "Progressive Damage and Fracture of Unstiffened and Stiffened Composite Pressure Vessels," *Journal of Reinforced Plastics and Composites*, Vol.16, pp. 1711-1724, 1997.
- [28] J. Triplett, J. Patterson, J. R. Esslinger and J. Zalameda, "Impact Damage Evaluation of Stiffened Graphite Epoxy Cylinders," *American Institute of Aeronautics and Astronautics*, AIAA-98-1787, pp.1809-1813, 1998.
- [29] R. Veys, A. Cederberg and J. Schimenti, "Fatigue Analysis Techniques for Composite Tankage with Plastically Operating Aluminum Liners," *AIAA, SAE, ASME, and ASEE, Joint Propulsion Conference, 27th*, Sacramento, CA; United States; Vol.8, pp.24-26, 1991.
- [30] B. Su and G. S. Bhuyan, "Fracture Analyses on the All-metal Cylinders and the Metal-lined Hoop-wrapped Cylinders with Axial Cracks," *The International Journal of Pressure Vessels and Piping*, Vol.76, pp.677-684, 1999.
- [31] C. Kaynak and O. Mat, "Uniaxial Fatigue Behavior of Filament-wound Glass-fiber/epoxy Composite Tubes," *Composites Science and Technology*, Vol. 61, pp. 1833-1840, 2001.
- [32] N. Tarakc, L. Gemi and A. Yapici, "Fatigue Failure Behavior of Glass/epoxy  $\pm 55$  Filament Wound Pipes under Internal Pressure," *Composites Science and Technology*, Vol.65, pp.703-708, 2005.
- [33] A. R. Shahani and M. M. Kheirikhah, "Stress Intensity Factor Calculation of Steel-lined Hoop-wrapped Cylinders with Internal Semi-elliptical Circumferential Crack," *Engineering Fracture Mechanics*, Vol.74, pp. 2004-2013, 2007.
- [34] M. A. Guerrero, C. Betegon and J. Belzunce, "Fracture Analysis of a Pressure Vessel Made of High Strength Steel (HSS)," *Engineering Failure Analysis*, Vol.15, pp.208-219, 2008.

## VITA

Jianbing Hu was born on August 24th, 1979 in Xiaogan, Hubei, People's Republic China. He joined Wuhan University of Technology, in Wuhan, China and obtained his B.E. degree in Mechanical Engineering in 2000. He then joined Huazhong University of Science & Technology, in Hubei, China in 2001 and obtained his M.S. degree in Mechanical Engineering in 2004. Jianbing Hu later enrolled for his Ph.D. in Mechanical Engineering at Missouri S&T since August 2004. He has held the position of Graduate Teaching Assistant since August 2004 to May 2005 at Missouri S&T in the Department of Mechanical and Aerospace Engineering and also held the position of Graduate Research Assistant since August 2004 to December 2008. He obtained his Ph.D. degree in Mechanical Engineering in Spring 2009 at Missouri S&T.